Commun Nonlinear Sci Numer Simulat 135 (2024) 108054

Contents lists available at ScienceDirect

Communications in Nonlinear Science and Numerical Simulation

journal homepage: www.elsevier.com/locate/cnsns

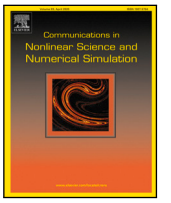

Research paper

Efficient second-order accurate scheme for fluid–surfactant systems on curved surfaces with unconditional energy stability

Bing Jiang [a], Qing Xia [a], Junseok Kim [b], Yibao Li [a,*]

[a] School of Mathematics and Statistics, Xi'an Jiaotong University, Xi'an 710049, China
[b] Department of Mathematics, Korea University, Seoul 02841, Republic of Korea

ARTICLE INFO

Keywords:
Triangular surface mesh
Unconditional energy stability
Scalar auxiliary variable
Fluid–surfactant system
Phase-field model

ABSTRACT

Accurately simulating the interplay between fluids and surfactants is a challenge, especially when ensuring both mass conservation and guaranteed energy stability. This study proposes a highly accurate numerical scheme for the water–oil–surfactant system coupled with the Navier–Stokes equation. We use the second-order accurate discrete operators on triangular grids representing these surfaces. We use the Crank–Nicolson method to achieve the second-order temporal accuracy. To handle high-order nonlinearities, we employ the consistency-enhanced Scalar Auxiliary Variable method. Additionally, the projection method tackles the Navier–Stokes equations. These techniques guarantee the unconditional stability. Consequently, larger time steps are permissible. Our method achieves the high accuracy with lower computational cost. This efficiency stems from solely utilizing surface information, eliminating the need for calculations across the entire 3D space. The proposed scheme's accuracy, stability, and robustness can be confirmed through various numerical experiments.

1. Introduction

Surfactants play vital roles across various domains, from everyday applications to advanced fields like medicine [1], chemical engineering [2–4], and biological sciences [5,6]. Their versatility stems from a unique molecular structure, characterized by a hydrophilic (water-attracting) group at one end and a hydrophobic (water-repelling) group at the other. When introduced into multiphase systems, surfactants significantly alter the dynamic between oil and water [7,8]. The hydrophilic end is drawn to water molecules, while the hydrophobic end seeks refuge within the oil phase [9,10]. This affinity allows surfactants to lower surface tension, enabling easier mixing and formation of stable oil-in-water emulsions [11]. Despite their widespread use and importance, accurately modeling and numerically simulating systems involving surfactants pose significant challenges [12]. The intricacies of interactions between surfactants, oil, and water, along with the dynamic nature of multiphase systems, make it difficult to develop precise computational models [13]. Additionally, the introduction of highly accurate and unconditionally energy-stable numerical schemes further complicates the task, requiring sophisticated algorithms and computational resources to tackle the complexities involved.

The phase field paradigm has been extensively harnessed to simulate fluid–surfactant interactions. The Cahn–Hilliard (CH) formulation [14] serves as a cornerstone for a growing volume of research in this domain [15–18]. Pioneering work by Laradji et al. [19] marked the initial application of the phase field methodology to encapsulate the dynamics of microemulsion systems. Subsequent studies, such as those by van der Graaf and Samn [20], delved into diffuse interface models, focusing on phenomena

* Corresponding author.
E-mail address: yibaoli@xjtu.edu.cn (Y. Li).
URL: http://gr.xjtu.edu.cn/web/yibaoli (Y. Li).

https://doi.org/10.1016/j.cnsns.2024.108054
Received 22 December 2023; Received in revised form 27 April 2024; Accepted 29 April 2024
Available online 3 May 2024

like droplet fragmentation and surfactant adsorption. Teng and Chern [21] advanced this field by formulating a phase field model that analyzed steady-state solutions for one-dimensional planar interfaces in the presence of surfactants. Zhu et al. [22] further addressed the complexity of the phase-field surfactant system by innovatively employing multiple scalar auxiliary variables (SAVs) to reformulate the governing equations. This approach led to a decoupled numerical methodology that guarantees energy stability. Building on this foundation, Xu et al. [23] introduced a stabilized-SAV numerical approach tailored for binary fluid–surfactant systems. This approach offered both second-order temporal precision and unconditional energy stability. Inspired by this framework, Yang et al. [24,25] developed a linear, decoupled scheme for the phase-field surfactant model. When combined with the Stabilized-SAV (S-SAV) method, this scheme was proven to uphold unconditional energy stability.

Simultaneously, numerous researchers have endeavored to couple the incompressible Navier–Stokes (NS) equations with the water–oil–surfactant system. Kim et al. [26] developed a fully implicit scheme with second-order accuracy for the Cahn–Hilliard–Navier–Stokes (CHNS) system. A multigrid iterative solver and the projection method [27] are employed to tackle the nonlinear terms and separate the pressure term, respectively. Zhu and Chen [28] developed several semi-explicit schemes for systems that involve multiphase with surfactants coupled with incompressible fluid flows. With the first-order scheme, they demonstrated its unconditional energy dissipation. Olshanskii et al. [29,30] developed a trace finite element method and introduced a Lagrange multiplier to ensure tangential vector field constraints on surfaces. Wang et al. [31] recently introduced an innovative energy-stable nonlinear scheme designed to address the fluid surfactant model with a moving contact line. Sun considered the curvature effects to introduce a binary fluid–surfactant phase field model [32] and investigated its impact on the dynamics of phase separation in the system. Pan et al. [33] solved the numerical approximation problem of binary surfactant phase field models on complex surfaces using the IGA-EIEQ method, which provides linearity, decoupling, unconditional energy stability, and second-order time accuracy. Furthermore, Sun et al. [34] coupled the NS equation with the established fluid–surfactant model and demonstrated its first-order unconditional energy stability. Huang et al. [35] addressed the challenges of conditional stability and numerical stiffness caused by small interfacial parameters in the evolving surface binary fluid–surfactant phase field model by employing stabilizing methods and an adaptive time-stepping technique. In [36], Xia et al. examined a comprehensive phase field model for fluid flow on curved surfaces. They integrated the temperature field into recent systems and implemented a second-order unconditionally stable scheme in [37]. Nonetheless, there remains a paucity of research concerning high-order stable schemes that couple NS equations with fluid–surfactant phase field models on curved surfaces.

This study presents an efficient numerical scheme to simulate the intricate evolution of a binary fluid–surfactant system on curved surfaces. This scheme achieves high accuracy and unconditional stability. We achieve this by coupling the well-established water–oil–surfactant system, describing fluid mixing, with the Navier–Stokes (NS) equations, governing fluid flow. The Crank–Nicolson method ensures second-order accuracy in time. Discretization is performed using the recently developed consistency-enhanced Scalar Auxiliary Variable (SAV) method [38]. This method is transformed into a readily solvable linear system using the Picard iteration technique. Importantly, these discrete systems are proven to be unconditionally stable, allowing for larger time steps in simulations. The proposed method stands out from alternatives by achieving high accuracy with minimal computational cost. This efficiency is achieved by utilizing only surface information, eliminating the need for calculations throughout the entire 3D space. Consequently, larger time steps are permissible. The effectiveness of our model is validated through various numerical experiments, showcasing its practicality and significance. The main contributions can be summarized as the following:

- We present the second-order unconditionally energy stable schemes based on the scalar auxiliary variable method for the fluid–surfactant computation on arbitrary surfaces.
- We prove the unconditional energy stability of the proposed method to validate that a larger time step can be used for the convergent solution.
- The defined discrete operator on the surface mesh is closed and the proposed numerical algorithm is readily implementable.

The remaining sections of this article are structured as follows: In Section 2, we develop a fluid–surfactant model applicable to arbitrary curved surface. Section 3 gives a comprehensive exposition of our scheme. Section 4 presents a multitude of computational tests. The paper concludes in Section 5.

2. Fluid–surfactant system on arbitrarily curved surfaces

To establish notations, we denote the inner product between functions $\phi(\mathbf{x})$ and $\psi(\mathbf{x})$ as $(\phi(\mathbf{x}),\psi(\mathbf{x}))_S = \int_S \phi(\mathbf{x})\psi(\mathbf{x})\mathrm{d}\mathbf{x}$ and the norm of function $\phi(\mathbf{x})$ as $\|\phi(\mathbf{x})\|_S^2 = (\phi(\mathbf{x}),\phi(\mathbf{x}))_S$, where $S \subset \mathbb{R}^3$ represents a fixed curved surface. We will examine the dimensionless system for fluid–surfactant, which is composed of water–oil–surfactant system and the Navier–Stokes equations, on S as:

$$\partial_t\phi(\mathbf{x},t) + \nabla_S\cdot(\phi(\mathbf{x},t)\mathbf{v}(\mathbf{x},t)) = M_\phi\Delta_S\mu_\phi(\mathbf{x},t), \tag{1a}$$

$$\mu_\phi(\mathbf{x},t) = F'(\phi(\mathbf{x},t)) - \varepsilon^2\Delta_S\phi(\mathbf{x},t) + \varepsilon\Big(\theta\nabla_S\cdot(\psi(\mathbf{x},t)\nabla_S\phi(\mathbf{x},t)) - \xi\nabla_S\cdot(|\nabla_S\phi(\mathbf{x},t)|^2\nabla_S\phi(\mathbf{x},t))\Big), \tag{1b}$$

$$\partial_t\psi(\mathbf{x},t) + \nabla_S\cdot(\psi(\mathbf{x},t)\mathbf{v}(\mathbf{x},t)) = M_\psi\Delta_S\mu_\psi(\mathbf{x},t), \tag{1c}$$

$$\mu_\psi(\mathbf{x},t) = G'(\psi(\mathbf{x},t)) - \gamma^2\Delta_S\psi(\mathbf{x},t) - \frac{\gamma\theta}{2}|\nabla_S\phi(\mathbf{x},t)|^2, \tag{1d}$$

$$\partial_t\mathbf{v}(\mathbf{x},t) + \frac{1}{2}\left(\nabla_S\cdot\big(\mathbf{v}(\mathbf{x},t)\otimes\mathbf{v}(\mathbf{x},t)\big) + \mathbf{v}(\mathbf{x},t)\cdot\nabla_S\mathbf{v}(\mathbf{x},t)\right)$$

$$= -\nabla_S p(\mathbf{x},t) + \nabla_S \cdot (\nu \nabla_S \mathbf{v}(\mathbf{x},t)) - \frac{\sigma}{\varepsilon}\phi(\mathbf{x},t)\nabla_S \mu_\phi(\mathbf{x},t) - \frac{\sigma}{\gamma}\psi(\mathbf{x},t)\nabla_S \mu_\psi(\mathbf{x},t), \tag{1e}$$

$$\nabla_S \cdot \mathbf{v}(\mathbf{x},t) = 0. \tag{1f}$$

Here ∇_S, and $\nabla_S \cdot$ denote the tangential gradient and divergence operators, respectively. Δ_S and $\otimes$ denote the tangential Laplace–Beltrami operator and tensor product, respectively. The phase field variable $\phi(\mathbf{x},t)$ represents the local component distribution within the binary fluid, where a value of 1 denotes one component, and 0 denotes the other one. The variable $\psi(\mathbf{x},t)$ indicates the concentration of the surfactant, ranging from 0 to 1. $\mu(\mathbf{x},t)$ and $p(\mathbf{x},t)$ represent the chemical potential and the pressure, respectively. The parameter ν denotes the viscosity. Due to the incompressible condition, which implies that $\nabla_S(\mathbf{v}\otimes\mathbf{v}) = \mathbf{v}\cdot\nabla_S\mathbf{v}$ when $\nabla_S \cdot \mathbf{v} = 0$, we derive the nonlinear advection term using formulation $\mathbf{v}\cdot\nabla_S\mathbf{v}/2 + \nabla_S(\mathbf{v}\otimes\mathbf{v})/2$. This equivalent substitution proves convenient for demonstrating energy dissipation while mitigating the stiffness effects introduced by the convection terms. Furthermore, the dimensionless parameters ε and γ represent the interface width between two phase-field variables, M_ϕ and M_ψ denote the mobility parameters, respectively. Additionally, σ represents the surface tension coefficient, and ξ and θ denote the intensities of coupled entropy energy, respectively. Especially, in the context of this paper, boundary conditions have not been specified for the system, since the focus is on fixed closed surfaces with enclosed properties. Considering the interaction between phase field variables and surfactant [32], we define the total energy functional [36,39–41] of the binary fluid–surfactant system as:

$$E = \int_S \left(\frac{1}{2}|\mathbf{v}|^2 + \frac{\varepsilon\sigma}{2}|\nabla_S\phi|^2 + \frac{\sigma}{\varepsilon}F(\phi) + \frac{\gamma\sigma}{2}|\nabla_S\psi|^2 + \frac{\sigma}{\gamma}G(\psi) + \sigma\left(\frac{\xi}{4}|\nabla_S\phi|^4 - \frac{1}{2}\theta\psi|\nabla_S\phi|^2\right)\right)\mathrm{d}\mathbf{x}, \tag{2}$$

where $F(\phi)$ and $G(\psi)$ represent the double well bulk energy functions, specifically describing hydrophobic interactions with the given formulas $F(\phi) = \phi^2(1-\phi)^2/4$ and $G(\psi) = \psi^2(1-\psi)^2/4$. In order to design an efficient numerical method, we initially define two auxiliary variables based on the SAV approach:

$$r(t) = \sqrt{H(\phi,\psi) + C} := \sqrt{\int_S \left(\frac{\sigma}{\varepsilon}F(\phi) + \frac{\sigma}{\gamma}G(\psi) + \sigma\left(\frac{\xi}{4}|\nabla_S\phi|^4 - \frac{1}{2}\theta\psi|\nabla_S\phi|^2\right)\right)\mathrm{d}\mathbf{x} + C}.$$

We introduce a nonlocal variable $Q(t)$, which is the solution to the following ordinary differential equation:

$$\begin{aligned} Q_t = \int_S \Big(& \nabla_S\cdot(\mathbf{v}\phi)\mu_\phi + \nabla_S\cdot(\mathbf{v}\psi)\mu_\psi + \phi\nabla_S\mu_\phi\cdot\mathbf{v} + \psi\nabla_S\mu_\psi\cdot\mathbf{v} \\ & + \frac{1}{2}\left(\nabla_S\cdot(\mathbf{v}\otimes\mathbf{v}) + \mathbf{v}\cdot\nabla_S\mathbf{v}\right)\cdot\mathbf{v}\Big)\,\mathrm{d}\mathbf{x}, \\ Q|_{t=0} = 1. & \end{aligned}$$

Through the utilization of Eq. (1f), the aforementioned ordinary differential equation can be deduced to be equivalent to $Q(t) \equiv 1$ via the application of integration by parts technique and leveraging the inherent property of "zero-energy-contribution" pertaining to both the convection term and surface tension [42,43]. In the continuous version, this procedure is straightforward as Q_t is consistently zero. Conversely, in the discrete version, such a procedure notably mitigates disturbances arising from the nonlinear term, facilitating the demonstration of unconditional energy stability [44,45]. The original model, Eqs. (1a)–(1f), is reformulated into the following equivalent forms

$$\phi_t + Q\nabla_S\cdot(\mathbf{v}\phi) = M_\phi\Delta_S\mu_\phi, \tag{3a}$$

$$\mu_\phi = -\varepsilon^2\Delta_S\phi + Ur, \tag{3b}$$

$$\psi_t + Q\nabla_S\cdot(\mathbf{v}\psi) = M_\psi\Delta_S\mu_\psi, \tag{3c}$$

$$\mu_\psi = -\gamma^2\Delta_S\psi + Vr, \tag{3d}$$

$$\mathbf{v}_t + \frac{Q}{2}\left(\mathbf{v}\cdot\nabla_S\mathbf{v} + \nabla_S\cdot(\mathbf{v}\otimes\mathbf{v})\right) = -\nabla_S p + \nabla_S\cdot(\nu\nabla_S\mathbf{v}) - \frac{Q\sigma}{\varepsilon}\phi\nabla_S\mu_\phi - \frac{Q\sigma}{\gamma}\psi\nabla_S\mu_\psi, \tag{3e}$$

$$\nabla_S\cdot\mathbf{v} = 0, \tag{3f}$$

$$r_t = \frac{1}{2}\left(\frac{\sigma}{\varepsilon}(U,\phi_t)_S + \frac{\sigma}{\gamma}(V,\psi_t)_S\right), \tag{3g}$$

$$\begin{aligned} Q_t = & \left(\nabla_S\cdot(\mathbf{v}\phi),\mu_\phi\right)_S + \left(\nabla_S\cdot(\mathbf{v}\psi),\mu_\psi\right)_S + \frac{1}{2}\left(\nabla_S\cdot(\mathbf{v}\otimes\mathbf{v}) + \mathbf{v}\cdot\nabla_S\mathbf{v},\mathbf{v}\right)_S \\ & + \left(\phi\nabla_S\mu_\phi,\mathbf{v}\right)_S + \left(\psi\nabla_S\mu_\psi,\mathbf{v}\right)_S, \end{aligned} \tag{3h}$$

where

$$U = \frac{F'(\phi) + \varepsilon\left(\theta\nabla_S\cdot(\psi\nabla_S\phi) - \xi\nabla_S\cdot(|\nabla_S\phi|^2\nabla_S\phi)\right)}{\sqrt{\int_S\left(\frac{\sigma}{\varepsilon}F(\phi) + \frac{\sigma}{\gamma}G(\psi) + \sigma\left(\frac{\xi}{4}|\nabla_S\phi|^4 - \frac{1}{2}\theta\psi|\nabla_S\phi|^2\right)\right)\mathrm{d}\mathbf{x} + C}},$$

$$V = \frac{G'(\psi) - \frac{\gamma\theta}{2}|\nabla_S\phi|^2}{\sqrt{\int_S\left(\frac{\sigma}{\varepsilon}F(\phi) + \frac{\sigma}{\gamma}G(\psi) + \sigma\left(\frac{\xi}{4}|\nabla_S\phi|^4 - \frac{1}{2}\theta\psi|\nabla_S\phi|^2\right)\right)\mathrm{d}\mathbf{x} + C}}.$$

Theorem 1. *The equivalent governing Eqs. (3a)–(3h) comply with the subsequent energy dissipation law*

$$\frac{d}{dt}E(\phi,\psi,\mathbf{v},r)\le 0,$$

where

$$E(\phi,\psi,\mathbf{v},r)=\int_S\left(\frac{1}{2}|\mathbf{v}|^2+\frac{\varepsilon\sigma}{2}|\nabla_S\phi|^2+\frac{\gamma\sigma}{2}|\nabla_S\psi|^2\right)d\mathbf{x}+r^2-C.$$

Proof. Taking the inner product of Eq. (3a) with $\frac{\sigma}{\varepsilon}\mu_\phi$ and taking integration by parts and combining Eq. (3b), we can obtain

$$\begin{aligned}\frac{\sigma}{\varepsilon}(\mu_\phi,\phi_t)_S=&\frac{Q\sigma}{\varepsilon}(\mathbf{v}\phi,\nabla_S\mu_\phi)_S-\frac{\sigma}{\varepsilon}M_\phi\|\nabla_S\mu_\phi\|_S^2\\=&-\varepsilon\sigma(\Delta_S\phi,\phi_t)_S+\frac{\sigma}{\varepsilon}(Ur,\phi_t)_S\\=&\frac{d}{dt}\int_S\frac{\varepsilon\sigma}{2}|\nabla_S\phi|^2d\mathbf{x}+\frac{\sigma}{\varepsilon}(Ur,\phi_t)_S.\end{aligned}\tag{4}$$

Similarly, taking the inner product of Eq. (3c) with $\frac{\sigma}{\gamma}\mu_\psi$ and taking integration by parts and combining Eq. (3d), we get

$$\begin{aligned}\frac{\sigma}{\gamma}(\mu_\psi,\psi_t)_S=&\frac{Q\sigma}{\gamma}(\mathbf{v}\psi,\nabla_S\mu_\psi)_S-\frac{\sigma}{\gamma}M_\psi\|\nabla_S\mu_\psi\|_S^2\\=&-\gamma\sigma(\Delta_S\psi,\psi_t)_S+\frac{\sigma}{\gamma}(Vr,\psi_t)_S\\=&\frac{d}{dt}\int_S\frac{\gamma\sigma}{2}|\nabla_S\psi|^2d\mathbf{x}+\frac{\sigma}{\gamma}(Vr,\psi_t)_S.\end{aligned}\tag{5}$$

Taking the inner product of Eq. (3e) with $\mathbf{v}$, we can obtain

$$(\mathbf{v},\mathbf{v}_t)_S=-\nu\|\nabla\mathbf{v}\|_S^2-\frac{Q}{2}\left(\mathbf{v}\cdot\nabla_S\mathbf{v}+\nabla_S\cdot(\mathbf{v}\otimes\mathbf{v}),\mathbf{v}\right)_S-\frac{Q\sigma}{\varepsilon}(\phi\nabla_S\mu_\phi,\mathbf{v})_S-\frac{Q\sigma}{\gamma}(\psi\nabla\mu_\psi,\mathbf{v})_S.\tag{6}$$

By combining Eqs. (4)–(6), Theorem 1 can be derived as follows:

$$\begin{aligned}\frac{\mathrm{d}}{\mathrm{d}t}E(\phi,\psi,\mathbf{v},r)=&\frac{d}{dt}\left(\int_S(\frac{1}{2}|\mathbf{v}|^2+\frac{\varepsilon\sigma}{2}|\nabla_S\phi|^2+\frac{\gamma\sigma}{2}|\nabla_S\psi|^2)\mathrm{d}\mathbf{x}+r^2-C\right)\\=&-\nu\|\nabla_S\mathbf{v}\|_S^2-M_\phi\|\nabla_S\mu_\phi\|_S^2-M_\psi\|\nabla_S\mu_\psi\|_S^2\le 0,\end{aligned}\tag{7}$$

which completes the proof. □

3. Numerical scheme for fluid–surfactant system on curved surface

3.1. Spatial operators on discrete surfaces

First, we present a spatial discretization approach for the proposed fluid–surfactant model on the surface. In fact, we need to introduce the formulas for operators(such as $\nabla_S,\nabla_S\cdot$, and Δ_S) on the surface in the discrete triangular mesh, which are represented by $\nabla_h,\nabla_h\cdot$, and Δ_h, respectively. For a given mesh $\Sigma:=(X,F)$ consisting of N_X vertices and N_T triangles, where $X=\{\mathbf{x}_i|1\le i\le N_X\}$ is the set of all vertices, and $F=\{T_i|1\le i\le N_T\}$ is the set of all triangles. As shown in Fig. 1, we focus on a specific vertex $\mathbf{x}\in X$. This vertex has a 1-ring neighborhood, denoted by the red circle, consisting of its directly connected neighboring vertices. Assuming that $\mathbf{x}$ is surrounded by s vertices, denoted as $\mathbf{x}_j$ (for $j=1,2,\dots,s$) and $\mathbf{x}_{s+1}=\mathbf{x}_1$. Let $G_j=(\mathbf{x}+\mathbf{x}_j+\mathbf{x}_{j+1})/3$ be the centroid of the triangle T_j with vertices $\mathbf{x},\mathbf{x}_j$ and $\mathbf{x}_{j+1}$. Then, as shown in Fig. 1, the green triangle is composed by the vertices $\mathbf{x}_j,\mathbf{G}_j$, and $\mathbf{G}_{j+1}$. The mesh formed in this way is called the dual mesh of Σ. Then, to achieve second-order accuracy, for any scalar-valued function $\boldsymbol{\Phi}$, we can define $\nabla_h\boldsymbol{\Phi}(\mathbf{G}_j)$ as follows [36]:

$$\nabla_h\boldsymbol{\Phi}(\mathbf{G}_j)=\alpha_j(\mathbf{x}_j-\mathbf{G}_j)+\beta_j(\mathbf{x}_{j+1}-\mathbf{G}_j).\tag{8}$$

Here α_j and β_j satisfy the following matrix equation:

$$\begin{pmatrix}\langle\mathbf{x}_j-\mathbf{G}_j,\mathbf{x}-\mathbf{G}_j\rangle & \langle\mathbf{x}_{j+1}-\mathbf{G}_j,\mathbf{x}-\mathbf{G}_j\rangle & \left\|\mathbf{x}-\mathbf{G}_j\right\|^2\\ \langle\mathbf{x}_j-\mathbf{G}_j,\mathbf{x}_j-\mathbf{G}_j\rangle & \langle\mathbf{x}_{j+1}-\mathbf{G}_j,\mathbf{x}_j-\mathbf{G}_j\rangle & \left\|\mathbf{x}_j-\mathbf{G}_j\right\|^2\\ \langle\mathbf{x}_j-\mathbf{G}_j,\mathbf{x}_{j+1}-\mathbf{G}_j\rangle & \langle\mathbf{x}_{j+1}-\mathbf{G}_j,\mathbf{x}_{j+1}-\mathbf{G}_j\rangle & \left\|\mathbf{x}_{j+1}-\mathbf{G}_j\right\|^2\end{pmatrix}\begin{pmatrix}\alpha_j\\ \beta_j\\ 0.5\Delta_h\boldsymbol{\Phi}(\mathbf{G}_j)\end{pmatrix}=\begin{pmatrix}\boldsymbol{\Phi}(\mathbf{x})-\boldsymbol{\Phi}(\mathbf{G}_j)\\ \boldsymbol{\Phi}(\mathbf{x}_j)-\boldsymbol{\Phi}(\mathbf{G}_j)\\ \boldsymbol{\Phi}(\mathbf{x}_{j+1})-\boldsymbol{\Phi}(\mathbf{G}_j)\end{pmatrix}.\tag{9}$$

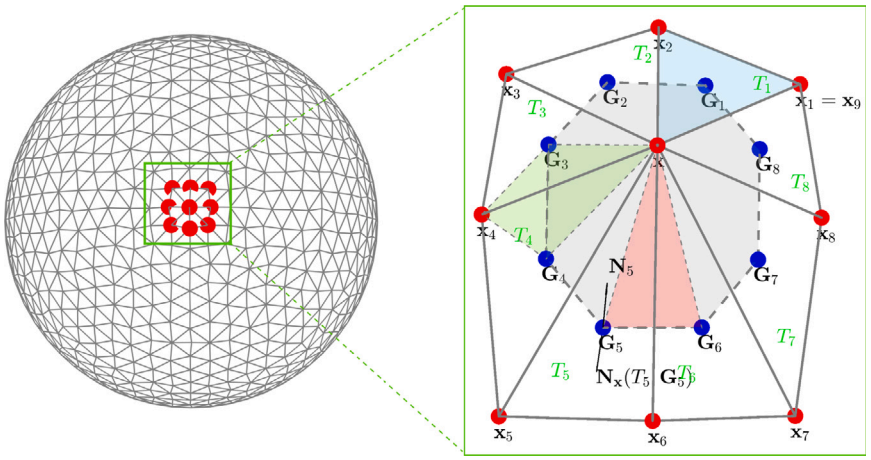

Fig. 1. An illustration of the scheme depicting the dual mesh adjacent to the vertex $\mathbf{x}$. The red point signifies a specific point $\mathbf{x}$ along with its adjacent points $\mathbf{x}_j$ within the initial grid. The blue point, G_i, denotes the geometric center of neighboring grids, illustrated by blue triangles. The green triangles symbolize the composition within the dual mesh.

Utilizing the Green function, the Laplace–Beltrami operator can be approximated as follows:

$$\begin{aligned}\Delta_h \boldsymbol{\Phi}(\mathbf{x}) = &\frac{1}{A(\mathbf{x})}\sum_{j=1}^{s+1}\frac{\left\|\mathbf{G}_{j+1}-\mathbf{G}_j\right\|}{6}\left(2\left\langle\nabla_h\boldsymbol{\Phi}\left(\mathbf{G}_j\right),\mathbf{n}_\mathbf{x}\left(T_j,\mathbf{G}_j\right)\right\rangle\right.\\ &+2\left\langle\nabla_h\boldsymbol{\Phi}\left(\mathbf{G}_{j+1}\right),\mathbf{n}_\mathbf{x}\left(T_j,\mathbf{G}_{j+1}\right)\right\rangle+\left\langle\nabla_h\boldsymbol{\Phi}\left(\mathbf{G}_j\right),\mathbf{n}_\mathbf{x}\left(T_j,\mathbf{G}_{j+1}\right)\right\rangle\\ &\left.+\left\langle\nabla_h\boldsymbol{\Phi}\left(\mathbf{G}_{j+1}\right),\mathbf{n}_\mathbf{x}\left(T_j,\mathbf{G}_j\right)\right\rangle\right),\end{aligned} \tag{10}$$

Here, $|\hat{T}_j|$ is the area of the triangle $\hat{T}_j$ composed of $\mathbf{x}$, $\mathbf{G}_j$, and $\mathbf{G}_{j+1}$, represented by the red color region in Fig. 1. Additionally, the total area $A(\mathbf{x})$ is given by $A(\mathbf{x}) = \sum_{j=1}^{s+1}|\hat{T}_j|$. The definitions of the outward normals $\mathbf{n}_\mathbf{x}(T_j,\mathbf{G}_j)$ and $\mathbf{n}_\mathbf{x}(T_j,\mathbf{G}_{j+1})$ are as follows:

$$\mathbf{n}_\mathbf{x}(T_j,\mathbf{G}_j)=\frac{(\mathbf{G}_{j+1}-G_j)\times\mathbf{N}_j}{\|(\mathbf{G}_{j+1}-G_j)\times\mathbf{N}_j\|}\ \text{and}\ \mathbf{n}_\mathbf{x}(T_j,\mathbf{G}_{j+1})=\frac{(\mathbf{G}_{j+1}-G_j)\times\mathbf{N}_{j+1}}{\|(\mathbf{G}_{j+1}-G_j)\times\mathbf{N}_{j+1}\|}. \tag{11}$$

We can obtain a discrete divergence operator with second-order accuracy by

$$\begin{aligned}\nabla_h\cdot\boldsymbol{\Phi}(\mathbf{x}) = &\frac{1}{A(\mathbf{x})}\sum_{j=1}^{s+1}\frac{\|\mathbf{G}_{j+1}-\mathbf{G}_j\|}{6}\left(\,2\langle\boldsymbol{\Phi}(\mathbf{G}_j),\mathbf{n}_\mathbf{x}(T_j,\mathbf{G}_j)\rangle\right.\\ &\left.+\,2\langle\boldsymbol{\Phi}(\mathbf{G}_{j+1}),\mathbf{n}_\mathbf{x}(T_j,\mathbf{G}_{j+1})\rangle+\langle\boldsymbol{\Phi}(\mathbf{G}_j),\mathbf{n}_\mathbf{x}(T_j,\mathbf{G}_{j+1})\rangle+\langle\boldsymbol{\Phi}(\mathbf{G}_{j+1}),\mathbf{n}_\mathbf{x}(T_j,\mathbf{G}_j)\rangle\,\right),\end{aligned} \tag{12}$$

and the discrete gradient operator as

$$\nabla_h\boldsymbol{\Phi}(\mathbf{x})=\sum_{j=1}^{s+1}\frac{\|\mathbf{G}_j-\mathbf{x}\|^{-2}}{\sum_{k=1}^{s+1}\|\mathbf{G}_k-\mathbf{x}\|^{-2}}\nabla_h\boldsymbol{\Phi}(\mathbf{G}_j)-\sum_{j=1}^{s+1}\frac{\|\mathbf{G}_j-\mathbf{x}\|^{-2}}{2\sum_{k=1}^{s+1}\|\mathbf{G}_k-\mathbf{x}\|^{-2}}\Delta_h\boldsymbol{\Phi}(\mathbf{x})(\mathbf{G}_j-\mathbf{x}). \tag{13}$$

3.2. Numerical scheme with second-order temporal accuracy

In this subsection, we present the SAV-based Crank–Nicolson-type method for fluid–surfactant systems, including its numerical implementation steps and proof of energy dissipation. We first introduce a relaxation step that corrects for nonlinear terms and transient auxiliary variables to resolve the inconsistencies produced by the classical SAV method. Then, the discrete energy dissipation can be demonstrated using the proposed relaxation scheme.

Before proceeding that, we need to define the inner product in the proposed scheme on the curved surface. Assuming that ϕ_i and ψ_i are functions on surfaces, where ϕ_i represents $\phi(\mathbf{x}_i)$ and ψ_i represents $\psi(\mathbf{x}_i)$, respectively. At the vertex, the discrete inner products can be defined as $(\phi,\psi)_h := \sum_{\mathbf{x}_i\in X}\phi_i\psi_i A(\mathbf{x}_i)$ and $(\nabla_h\phi,\nabla_h\psi)_h := \sum_{\mathbf{x}_i\in X}\left(A(\mathbf{x}_i)\sum_{j=0}^{s-1}\nabla_h\phi(\mathbf{G}_j)\cdot\nabla_h\phi(\mathbf{G}_j)\right)$. The discrete norm of function ϕ can be deduced as $\|\phi\|_h^2=(\phi,\phi)_h$ and $\|\nabla_h\phi\|_h^2=(\nabla_h\phi,\nabla_h\phi)_h$, respectively. In the following content, we use a consistent time step length denoted as $\Delta t = T/N^T$, where T represents the total computation time and N^T stands for the number of iteration steps. Assuming the given initial conditions for ϕ_i^0,ψ_i^0,p_i^0 and $\mathbf{v}_i^0$, we consider that the solution at the first iteration satisfies $\phi_i^{-1}=\phi_i^0,\psi_i^{-1}=\psi_i^0$ and $\mathbf{v}_i^{-1}=\mathbf{v}_i^0$.

Step1. The Crank–Nicolson-type method is employed for the fluid–surfactant system to achieve the second-order accuracy. The proposed scheme can be described as follows:

$$\frac{\mathbf{v}^*-\mathbf{v}^n}{\Delta t}+\frac{\hat{Q}^{n+\frac{1}{2}}}{2}\left(\tilde{\mathbf{v}}^{n+\frac{1}{2}}\cdot\nabla_h\tilde{\mathbf{v}}^{n+\frac{1}{2}}+\nabla_h\cdot(\tilde{\mathbf{v}}^{n+\frac{1}{2}}\otimes\tilde{\mathbf{v}}^{n+\frac{1}{2}})\right)=-\nabla_h p^n+\nu\Delta_h\left(\frac{\mathbf{v}^*+\mathbf{v}^n}{2}\right)$$
$$-\frac{\sigma\hat{Q}^{n+\frac{1}{2}}}{\varepsilon}\tilde{\phi}^{n+\frac{1}{2}}\nabla_h\tilde{\mu}_\phi^{n+\frac{1}{2}}-\frac{\sigma\hat{Q}^{n+\frac{1}{2}}}{\gamma}\tilde{\psi}^{n+\frac{1}{2}}\nabla_h\tilde{\mu}_\psi^{n+\frac{1}{2}},\tag{14a}$$

$$\frac{\mathbf{v}^{n+1}-\mathbf{v}^*}{\Delta t}=-\frac{1}{2}(\nabla_h p^{n+1}-\nabla_h p^n),\tag{14b}$$

$$\nabla_h\cdot\mathbf{v}^{n+1}=0,\tag{14c}$$

$$\frac{\phi^{n+1}-\phi^n}{\Delta t}=M_\phi\Delta_h\mu_\phi^{n+\frac{1}{2}}-\hat{Q}^{n+\frac{1}{2}}\nabla_h\cdot(\tilde{\mathbf{v}}^{n+\frac{1}{2}}\tilde{\phi}^{n+\frac{1}{2}}),\tag{14d}$$

$$\mu_\phi^{n+\frac{1}{2}}=-\varepsilon^2\Delta_h\phi^{n+\frac{1}{2}}+\tilde{U}^{n+\frac{1}{2}}\hat{r}^{n+\frac{1}{2}}+S_\phi(\phi^{n+\frac{1}{2}}-\tilde{\phi}^{n+\frac{1}{2}}),\tag{14e}$$

$$\frac{\psi^{n+1}-\psi^n}{\Delta t}=M_\psi\Delta_h\mu_\psi^{n+\frac{1}{2}}-\hat{Q}^{n+\frac{1}{2}}\nabla_h\cdot(\tilde{\mathbf{v}}^{n+\frac{1}{2}}\tilde{\psi}^{n+\frac{1}{2}}),\tag{14f}$$

$$\mu_\psi^{n+\frac{1}{2}}=-\gamma^2\Delta_h\psi^{n+\frac{1}{2}}+\tilde{V}^{n+\frac{1}{2}}\hat{r}^{n+\frac{1}{2}}+S_\psi(\psi^{n+\frac{1}{2}}-\tilde{\psi}^{n+\frac{1}{2}}),\tag{14g}$$

$$\frac{\hat{r}^{n+1}-r^n}{\Delta t}=\frac{1}{2}\left(\frac{\sigma}{\varepsilon}\left(\tilde{U}^{n+\frac{1}{2}},\frac{\phi^{n+1}-\phi^n}{\Delta t}\right)_h+\frac{\sigma}{\gamma}\left(\tilde{V}^{n+\frac{1}{2}},\frac{\psi^{n+1}-\psi^n}{\Delta t}\right)_h\right),\tag{14h}$$

$$\frac{\hat{Q}^{n+1}-Q^n}{\Delta t}=\frac{\sigma}{\varepsilon}\left(\left(\nabla_h\cdot(\tilde{\mathbf{v}}^{n+\frac{1}{2}}\tilde{\phi}^{n+\frac{1}{2}}),\mu_\phi^{n+\frac{1}{2}}\right)_h+\left(\tilde{\phi}^{n+\frac{1}{2}}\nabla_h\tilde{\mu}_\phi^{n+\frac{1}{2}},\frac{\mathbf{v}^*+\mathbf{v}^n}{2}\right)_h\right)$$
$$+\frac{\sigma}{\gamma}\left(\left(\nabla_h\cdot(\tilde{\mathbf{v}}^{n+\frac{1}{2}}\tilde{\psi}^{n+\frac{1}{2}}),\mu_\psi^{n+\frac{1}{2}}\right)_h+\left(\tilde{\psi}^{n+\frac{1}{2}}\nabla_h\tilde{\mu}_\psi^{n+\frac{1}{2}},\frac{\mathbf{v}^*+\mathbf{v}^n}{2}\right)_h\right)$$
$$+\left(\frac{\left(\tilde{\mathbf{v}}^{n+\frac{1}{2}}\cdot\nabla_h\tilde{\mathbf{v}}^{n+\frac{1}{2}}+\nabla_h\cdot(\tilde{\mathbf{v}}^{n+\frac{1}{2}}\otimes\tilde{\mathbf{v}}^{n+\frac{1}{2}})\right)}{2},\frac{\mathbf{v}^*+\mathbf{v}^n}{2}\right)_h,\tag{14i}$$

where $(\tilde{\cdot})^{n+\frac{1}{2}}=\left(3(\cdot)^n-(\cdot)^{n-1}\right)/2$, and $(\cdot)^{n+\frac{1}{2}}=\left((\cdot)^{n+1}+(\cdot)^n\right)/2$. In this study, the momentum equation is discretized using the projection method with pressure correction in time [45]. The variable $\mathbf{v}^*$ denotes the intermediate velocity, and the variables $(\hat{\cdot})^{n+1}$ represent the auxiliary variables discretized in time without relaxation. Additionally, in the Eqs. (14e) and (14g), the last terms serves as stabilization mechanism.

While $r=\sqrt{H(\phi,\psi)+C}$ and $Q=1$ maintain consistency in continuous systems, their discrete counterparts $\hat{r}^{n+1}$ and $\hat{Q}^{n+1}$ results in $\hat{r}^{n+1}\neq\sqrt{H(\phi^{n+1},\psi^{n+1})+C}$ and $\hat{Q}^{n+1}$ not being constant. This drawback result in a loss of consistency in the modified discrete energy dissipation law. Moreover, in the discrete version represented by Eq. (14i), the right side is not consistently equal to 0, which results in the time-discretized $\hat{Q}^{n+1}$ being inconsistent with its exact value of 1. The definition provided in Eq. (14i) does not guarantee that the calculated $\hat{Q}^{n+1}$ will consistently remain close to 1 under various simulation parameters. At the same time, the consistency between the numerical approach and the underlying model can lead to unreliable simulations because of the deviation between the calculated $\hat{Q}^{n+1}$ and 1. To address these issues, the following relaxation step is proposed to correct for $\hat{r}^{n+1}$ inspired by the idea presented in [38,46].

Step2. After computing $\hat{r}^{n+1},r^n,\phi^{n+1},\psi^{n+1},\hat{Q}^{n+1},Q^n,\mu_\phi^{n+\frac{1}{2}}$, and $\mu_\psi^{n+\frac{1}{2}}$, we proceed to obtain the corrected value r^{n+1} from

$$r^{n+1}=\lambda_1\hat{r}^{n+1}+(1-\lambda_1)\sqrt{H(\phi^{n+1},\psi^{n+1})+C}.\tag{15}$$

Here,

$$\lambda_1\in[0,1],\quad\text{s.t.}\quad|r^{n+1}|^2-|\hat{r}^{n+1}|^2\le\Delta t\eta_1(\|\nabla\mu_\phi^{n+\frac{1}{2}}\|_h^2+\|\nabla\mu_\psi^{n+\frac{1}{2}}\|_h^2),\tag{16}$$

where $0<\eta_1<\min\{\frac{\sigma M_\phi}{\varepsilon},\frac{\sigma M_\psi}{\gamma}\}$. A simplified inequality can be obtained from above one

$$a_1\lambda_1^2+b_1\lambda_1+c_1\le0,$$

where the coefficients are

$$a_1=\left(\hat{r}^{n+1}-\sqrt{H(\phi^{n+1},\psi^{n+1})+C}\right)^2,$$
$$b_1=2\left(\hat{r}^{n+1}-\sqrt{H(\phi^{n+1},\psi^{n+1})+C}\right)\sqrt{H(\phi^{n+1},\psi^{n+1})+C},$$
$$c_1=-(\hat{r}^{n+1})^2+H(\phi^{n+1},\psi^{n+1})+C-\Delta t\eta_1(\|\nabla\mu_\phi^{n+\frac{1}{2}}\|_h^2+\|\nabla\mu_\psi^{n+\frac{1}{2}}\|_h^2).$$

Note that $a_1+b_1+c_1=-\Delta t\eta_1(\|\nabla\mu_\phi^{n+\frac{1}{2}}\|_h^2+\|\nabla\mu_\psi^{n+\frac{1}{2}}\|_h^2)\le0$, and $a_1\neq0$, the solution to this optimization problem should be:

$$\lambda_1=\max\{0,(-b_1-\sqrt{b_1^2-4a_1c_1})/2a_1\}.$$

Next, the corrected auxiliary variable Q^{n+1} can be obtained from

$$Q^{n+1} = \lambda_2 \hat{Q}^{n+1} + (1-\lambda_2). \tag{17}$$

Here,

$$\lambda_2 \in [0,1], \quad \text{s.t.} \quad \frac{1}{2}\left(|Q^{n+1}|^2 - |\hat{Q}^{n+1}|^2\right) \le \frac{1}{4}\Delta t \eta_2 \|\nabla(\mathbf{v}^* + \mathbf{v}^n)\|_h^2, \tag{18}$$

where $0 < \eta_2 \le \nu$. Similarly, a simplified inequality can be obtained from above one

$$a_2\lambda_2^2 + b_2\lambda_2 + c_2 \le 0,$$

where the coefficients are

$$a_2 = \left(\hat{Q}^{n+1} - 1\right)^2, \qquad b_2 = 2\left(\hat{Q}^{n+1} - 1\right),$$
$$c_2 = 1 - \hat{Q}^{n+1} - \frac{1}{2}\Delta t \eta_2 \|\nabla(\mathbf{v}^* + \mathbf{v}^n)\|_h^2.$$

Note that $a_2 + b_2 + c_2 = -\frac{1}{2}\Delta t \eta_2 \|\nabla(\mathbf{v}^* + \mathbf{v}^n)\|_h^2 \le 0$, and $a_2 \ne 0$, the solution to this optimization problem should be:

$$\lambda_2 = \max\{0, (-b_2 - \sqrt{b_2^2 - 4a_2c_2})/2a_2\}.$$

Remark 1. It is pertinent to note that within the confines of the present manuscript, due to constraints on length, we have elected to omit the detailed exposition pertaining to the proof of uniqueness and solvability for Eqs. (14a)–(14i). While the discrete system (14) is not fully decoupled into a linear system [45], the interested reader may refer to the methodology espoused in [24,25], where an analogous uniqueness and solvability analysis is conducted for a coupled system involving surfactant dynamics on surfaces with the Navier–Stokes equations utilizing the SAV approach [47]. We posit that the principles and techniques delineated therein can be judiciously adapted and applied to the context of our study, offering a foundational basis for ascertaining the mathematical rigor of our model.

3.3. Discrete energy stability

Before investigating the discrete energy stability, we should briefly review the following lemma, which has been proved in [36]:

Lemma 1. *Let $\Sigma := (X, F)$ be the triangular mesh without boundary and denote ϕ and ψ to be the vector field on Σ. We have*

$$(\Delta_h\phi, \psi)_h = -(\nabla_h\phi, \nabla_h\psi)_h. \tag{19}$$

Thus we can establish the following discrete energy stable theorem.

Theorem 2. *By taking Lemma 1, the solution of Eqs. (14a)–(14i), Eqs. (15) and (17) satisfy the energy dissipation property*

$$E^{n+1} - E^n \le 0, \tag{20}$$

where the discrete energy is

$$\begin{aligned} E^n =& \frac{\varepsilon\sigma}{2}\|\nabla_h\phi^n\|_h^2 + \frac{\sigma S_\phi}{4\varepsilon}\|\phi^n - \phi^{n-1}\|_h^2 + \frac{\gamma\sigma}{2}\|\nabla\psi^n\|_h^2 + \frac{\sigma S_\psi}{4\gamma}\|\psi^n - \psi^{n-1}\|_h^2 \\ &+ \frac{1}{2}\|\mathbf{v}^n\|_h^2 + \frac{\Delta t^2}{8}\|\nabla_h p^n\|_h^2 + |r^n|^2 - C + \frac{1}{2}|Q^n|^2 - \frac{1}{2}. \end{aligned}$$

Proof. Taking the inner product of Eq. (14d) with $\frac{\sigma\Delta t}{\varepsilon}\mu_\phi^{n+\frac{1}{2}}$ and combining with Lemma 1, we have

$$\frac{\sigma}{\varepsilon}(\mu_\phi^{n+\frac{1}{2}}, \phi^{n+1} - \phi^n)_h = -\frac{\sigma M_\phi \Delta t}{\varepsilon}\|\nabla_h\mu_\phi^{n+\frac{1}{2}}\|_h^2 - \frac{\sigma\Delta t}{\varepsilon}\left(\hat{Q}^{n+\frac{1}{2}}\nabla_h\cdot(\tilde{\mathbf{v}}^{n+\frac{1}{2}}\tilde{\phi}^{n+\frac{1}{2}}), \mu_\phi^{n+\frac{1}{2}}\right)_h. \tag{21}$$

Taking the inner product of Eq. (14e) with $\frac{\sigma}{\varepsilon}(\phi^{n+1} - \phi^n)$, we obtain

$$\begin{aligned} \frac{\sigma}{\varepsilon}(\mu_\phi^{n+\frac{1}{2}}, \phi^{n+1} - \phi^n)_h =& \frac{\varepsilon\sigma}{2}\left(\|\nabla_h\phi^{n+1}\|_h^2 - \|\nabla_h\phi^n\|_h^2\right) + \frac{\sigma}{\varepsilon}\left(\tilde{U}^{n+\frac{1}{2}}\hat{r}^{n+\frac{1}{2}}, \phi^{n+1} - \phi^n\right)_h \\ &+ \frac{\sigma S_\phi}{4\varepsilon}(\|\phi^{n+1} - \phi^n\|_h^2 - \|\phi^n - \phi^{n-1}\|_h^2 + \|\phi^{n+1} - 2\phi^n + \phi^{n-1}\|_h^2). \end{aligned} \tag{22}$$

Similarly, taking the inner product of Eq. (14f) with $\frac{\sigma\Delta t}{\gamma}\mu_\psi^{n+\frac{1}{2}}$, we have

$$\frac{\sigma}{\gamma}(\mu_\psi^{n+\frac{1}{2}}, \psi^{n+1} - \psi^n)_h = -\frac{\sigma M_\psi \Delta t}{\gamma}\|\nabla_h\mu_\psi^{n+\frac{1}{2}}\|_h^2 - \frac{\sigma\Delta t}{\gamma}\left(\hat{Q}^{n+\frac{1}{2}}\nabla_h\cdot(\tilde{\mathbf{v}}^{n+\frac{1}{2}}\tilde{\psi}^{n+\frac{1}{2}}), \mu_\psi^{n+\frac{1}{2}}\right)_h. \tag{23}$$

Taking the inner product of Eq. (14g) with $\frac{\sigma}{\gamma}(\psi^{n+1}-\psi^n)$, we can obtain

$$\begin{aligned}\frac{\sigma}{\gamma}(\mu_\psi^{n+\frac{1}{2}},\psi^{n+1}-\psi^n)_h =&\frac{\gamma\sigma}{2}\left(\|\nabla_h\psi^{n+1}\|_h^2-\|\nabla_h\psi^n\|_h^2\right)+\frac{\sigma}{\gamma}\left(\tilde{V}^{n+\frac{1}{2}}\hat{r}^{n+\frac{1}{2}},\psi^{n+1}-\psi^n\right)_h\\&+\frac{\sigma S_\psi}{4\gamma}(\|\psi^{n+1}-\psi^n\|_h^2-\|\psi^n-\psi^{n-1}\|_h^2+\|\psi^{n+1}-2\psi^n+\psi^{n-1}\|_h^2).\end{aligned}\tag{24}$$

By multiplying Eq. (14h) with $2\Delta t\hat{r}^{n+\frac{1}{2}}$, we have

$$\begin{aligned}|\hat{r}^{n+1}|^2-|r^n|^2=&2\Delta t\hat{r}^{n+\frac{1}{2}}\cdot\left(\frac{\hat{r}^{n+1}-r^n}{\Delta t}\right)\\=&\frac{\sigma}{\varepsilon}\left(\tilde{U}^{n+\frac{1}{2}}\hat{r}^{n+\frac{1}{2}},\phi^{n+1}-\phi^n\right)_h+\frac{\sigma}{\gamma}\left(\tilde{V}^{n+\frac{1}{2}}\hat{r}^{n+\frac{1}{2}},\psi^{n+1}-\psi^n\right)_h.\end{aligned}\tag{25}$$

Taking the inner product of Eq. (14a) with $\Delta t(\mathbf{v}^*+\mathbf{v}^n)/2$, we have

$$\begin{aligned}&\frac{1}{2}(\|\mathbf{v}^*\|_h^2-\|\mathbf{v}^n\|_h^2)+\frac{1}{2}\Delta t(\nabla_h p^n,\mathbf{v}^*+\mathbf{v}^n)_h\\=&-\frac{\nu\Delta t}{4}\|\nabla_h(\mathbf{v}^*+\mathbf{v}^n)\|_h^2-\frac{\hat{Q}^{n+\frac{1}{2}}\Delta t}{4}\left(\tilde{\mathbf{v}}^{n+\frac{1}{2}}\cdot\nabla_h\tilde{\mathbf{v}}^{n+\frac{1}{2}}+\nabla_h\cdot(\tilde{\mathbf{v}}^{n+\frac{1}{2}}\otimes\tilde{\mathbf{v}}^{n+\frac{1}{2}}),\mathbf{v}^*+\mathbf{v}^n\right)_h\\&-\frac{\sigma\Delta t}{2\varepsilon}(\hat{Q}^{n+\frac{1}{2}}\tilde{\phi}^{n+\frac{1}{2}}\nabla_h\tilde{\mu}_\phi^{n+\frac{1}{2}},\mathbf{v}^*+\mathbf{v}^n)_h-\frac{\sigma\Delta t}{2\gamma}(\hat{Q}^{n+\frac{1}{2}}\tilde{\psi}^{n+\frac{1}{2}}\nabla_h\tilde{\mu}_\psi^{n+\frac{1}{2}},\mathbf{v}^*+\mathbf{v}^n)_h.\end{aligned}\tag{26}$$

Recalling Eq. (14b), we find that

$$\frac{\mathbf{v}^{n+1}}{\Delta t}+\frac{1}{2}\nabla_h p^{n+1}=\frac{\mathbf{v}^*}{\Delta t}+\frac{1}{2}\nabla_h p^n.\tag{27}$$

Squaring the above equality and combining with Lemma 1 and Eq. (14c), we can obtain

$$\frac{1}{2}\Delta t(\nabla_h p^n,\mathbf{v}^*+\mathbf{v}^n)_h=\frac{1}{2}\|\mathbf{v}^{n+1}\|_h^2-\frac{1}{2}\|\mathbf{v}^*\|_h^2+\frac{\Delta t^2}{8}(\|\nabla p^{n+1}\|_h^2-\|\nabla p^n\|_h^2).\tag{28}$$

Combining Eqs. (26) and (28), we obtain

$$\begin{aligned}&\frac{1}{2}(\|\mathbf{v}^{n+1}\|_h^2-\|\mathbf{v}^n\|_h^2)+\frac{\Delta t^2}{8}(\|\nabla p^{n+1}\|_h^2-\|\nabla p^n\|_h^2)\\=&-\frac{\nu\Delta t}{4}\|\nabla_h(\mathbf{v}^*+\mathbf{v}^n)\|_h^2-\frac{\hat{Q}^{n+\frac{1}{2}}\Delta t}{4}\left(\tilde{\mathbf{v}}^{n+\frac{1}{2}}\cdot\nabla_h\tilde{\mathbf{v}}^{n+\frac{1}{2}}+\nabla_h\cdot(\tilde{\mathbf{v}}^{n+\frac{1}{2}}\otimes\tilde{\mathbf{v}}^{n+\frac{1}{2}}),\mathbf{v}^*+\mathbf{v}^n\right)_h\\&-\frac{\sigma\Delta t}{2\varepsilon}(\hat{Q}^{n+\frac{1}{2}}\tilde{\phi}^{n+\frac{1}{2}}\nabla_h\tilde{\mu}_\phi^{n+\frac{1}{2}},\mathbf{v}^*+\mathbf{v}^n)_h-\frac{\sigma\Delta t}{2\gamma}(\hat{Q}^{n+\frac{1}{2}}\tilde{\psi}^{n+\frac{1}{2}}\nabla_h\tilde{\mu}_\psi^{n+\frac{1}{2}},\mathbf{v}^*+\mathbf{v}^n)_h.\end{aligned}\tag{29}$$

Multiplying Eq. (14i) with $\Delta t\hat{Q}^{n+\frac{1}{2}}$, we have

$$\begin{aligned}\hat{Q}^{n+\frac{1}{2}}(\hat{Q}^{n+1}-Q^n)=&\frac{1}{2}\left(|\hat{Q}^{n+1}|^2-|Q^n|^2\right)\\=&+\frac{\sigma\Delta t}{\varepsilon}\left(\hat{Q}^{n+\frac{1}{2}}\nabla_h\cdot(\tilde{\mathbf{v}}^{n+\frac{1}{2}}\tilde{\phi}^{n+\frac{1}{2}}),\mu_\phi^{n+\frac{1}{2}}\right)_h+\frac{\sigma\Delta t}{2\varepsilon}(\hat{Q}^{n+\frac{1}{2}}\tilde{\phi}^{n+\frac{1}{2}}\nabla_h\tilde{\mu}_\phi^{n+\frac{1}{2}},\mathbf{v}^*+\mathbf{v}^n)_h\\&+\frac{\sigma\Delta t}{\gamma}\left(\hat{Q}^{n+\frac{1}{2}}\nabla_h\cdot(\tilde{\mathbf{v}}^{n+\frac{1}{2}}\tilde{\psi}^{n+\frac{1}{2}}),\mu_\psi^{n+\frac{1}{2}}\right)_h+\frac{\sigma\Delta t}{2\gamma}(\hat{Q}^{n+\frac{1}{2}}\tilde{\psi}^{n+\frac{1}{2}}\nabla_h\tilde{\mu}_\psi^{n+\frac{1}{2}},\mathbf{v}^*+\mathbf{v}^n)_h\\&+\frac{\hat{Q}^{n+\frac{1}{2}}\Delta t}{4}\left(\tilde{\mathbf{v}}^{n+\frac{1}{2}}\cdot\nabla_h\tilde{\mathbf{v}}^{n+\frac{1}{2}}+\nabla_h\cdot(\tilde{\mathbf{v}}^{n+\frac{1}{2}}\otimes\tilde{\mathbf{v}}^{n+\frac{1}{2}}),\mathbf{v}^*+\mathbf{v}^n\right)_h.\end{aligned}\tag{30}$$

Combining Eqs. (21)–(25) and (29)–(30), we get

$$\begin{aligned}&\frac{\varepsilon\sigma}{2}\left(\|\nabla_h\phi^{n+1}\|_h^2-\|\nabla_h\phi^n\|_h^2\right)+\frac{\gamma\sigma}{2}\left(\|\nabla_h\psi^{n+1}\|_h^2-\|\nabla_h\psi^n\|_h^2\right)\\&+\frac{\sigma S_\phi}{4\varepsilon}(\|\phi^{n+1}-\phi^n\|_h^2-\|\phi^n-\phi^{n-1}\|_h^2+\|\phi^{n+1}-2\phi^n+\phi^{n-1}\|_h^2)\\&+\frac{\sigma S_\psi}{4\gamma}(\|\psi^{n+1}-\psi^n\|_h^2-\|\psi^n-\psi^{n-1}\|_h^2+\|\psi^{n+1}-2\psi^n+\psi^{n-1}\|_h^2)\\&+\frac{1}{2}(\|\mathbf{v}^{n+1}\|_h^2-\|\mathbf{v}^n\|_h^2)+\frac{\Delta t^2}{8}(\|\nabla p^{n+1}\|_h^2-\|\nabla p^n\|_h^2)+|\hat{r}^{n+1}|^2-|r^n|^2\\=&-\frac{\sigma M_\phi\Delta t}{\varepsilon}\|\nabla_h\mu_\phi^{n+\frac{1}{2}}\|_h^2-\frac{\sigma M_\psi\Delta t}{\gamma}\|\nabla_h\mu_\psi^{n+\frac{1}{2}}\|_h^2-\frac{\nu\Delta t}{4}\|\nabla_h(\mathbf{v}^*+\mathbf{v}^n)\|_h^2-\frac{1}{2}\left(|\hat{Q}^{n+1}|^2-|Q^n|^2\right).\end{aligned}\tag{31}$$

By combining Eq. (31) with the inequality in Eq. (15) and Eq. (17) we can obtain the energy dissipation as follows:

$$\begin{aligned}
&E^{n+1}-E^{n}\\
=&\frac{\varepsilon\sigma}{2}\left(\|\nabla_h\phi^{n+1}\|_h^2-\|\nabla_h\phi^{n}\|_h^2\right)+\frac{\sigma S_\phi}{4\varepsilon}(\|\phi^{n+1}-\phi^{n}\|_h^2-\|\phi^{n}-\phi^{n-1}\|_h^2)\\
&+\frac{\gamma\sigma}{2}\left(\|\nabla_h\psi^{n+1}\|_h^2-\|\nabla_h\psi^{n}\|_h^2\right)+\frac{\sigma S_\psi}{4\gamma}(\|\psi^{n+1}-\psi^{n}\|_h^2-\|\psi^{n}-\psi^{n-1}\|_h^2)\\
&+\frac{1}{2}(\|\mathbf{v}^{n+1}\|_h^2-\|\mathbf{v}^{n}\|_h^2)+\frac{\Delta t^2}{8}(\|\nabla p^{n+1}\|_h^2-\|\nabla p^{n}\|_h^2)+|r^{n+1}|^2-|r^{n}|^2+\frac{1}{2}|Q^{n+1}-Q^{n}|^2\\
\le&-\left(\frac{\sigma M_\phi}{\varepsilon}-\eta_1\right)\Delta t\|\nabla_h\mu_\phi^{n+\frac{1}{2}}\|_h^2-\left(\frac{\sigma M_\psi}{\gamma}-\eta_1\right)\Delta t\|\nabla_h\mu_\psi^{n+\frac{1}{2}}\|_h^2-\frac{1}{4}(\nu-\eta_2)\Delta t\|\nabla_h(\mathbf{v}^{*}+\mathbf{v}^{n})\|_h^2\\
&-\frac{S_\phi}{2}\|\nabla\phi^{n+1}-2\nabla\phi^{n}+\nabla\phi^{n-1}\|_h^2-\frac{S_\psi}{2}\|\nabla\psi^{n+1}-2\nabla\psi^{n}+\nabla\psi^{n-1}\|_h^2\le 0,
\end{aligned}\tag{32}$$

which corresponds to Eq. (20). □

Remark 2. For the sake of brevity and clarity, it is imperative to elucidate that the discrete operators defined on the curved spatial domain within this work have been previously validated to possess analogous properties to those defined in conventional Euclidean spaces, as substantiated by the literature [36,48–50]. As a result, the convergence properties and error estimates that are well-established for discrete systems within standard Euclidean geometry are ostensibly applicable, and by extension, can be adapted to our context of curved spaces without the loss of generality. In light of this, while our investigation encompasses the dynamics of a fluid–surfactant system on a discretized surface, the fundamental algorithmic framework remains consistent with the principles that govern analogous systems in Euclidean domains. The robustness of the convergence and error estimation for the Surface-Active Agent (SAV) method has been thoroughly established and numerically corroborated in prior works [51–53]. Given the aforementioned reasons, a detailed convergence analysis specific to our proposed scheme is deemed redundant and is consequently not included herein. Moreover, we affirm that our algorithm exhibits second-order convergence in both spatial and temporal dimensions, as substantiated by our numerical validations.

4. Numerical tests

4.1. Mass conservation and energy dissipation test

In this subsection, we verify the unconditional stability of the proposed method. The subsequent discussion will illustrate the law of energy dissipation and mass conservation. Here are the initial conditions:

$$\begin{cases}\phi(x,y,z,0)=0.5+0.01(\text{rand}(x,y,z)-0.5),\\ \psi(x,y,z,0)=0.1+0.05\text{rand}(x,y,z),\\ u(x,y,z,0)=0.02,\quad v(x,y,z,0)=0,\quad w(x,y,z,0)=0,\quad p(x,y,z,0)=0,\end{cases}$$

where rand (x,y,z) represents a random number ranging from 0 to 1. We employ the following set of parameter values for the numerical simulations: $h=0.1$, $\varepsilon=\gamma=0.02$, $M_\phi=M_\psi=0.02$, $\sigma=\varepsilon$, $\xi=0.0001$, $\theta=0.03$, $\nu=1$. As shown in Fig. 2, we can observe the phase separation of the phase field variables ϕ and surfactant ψ from the initial chaotic state with the influence of the fluid–surfactant model. Due to surface tension, the interface visibly evolves, with a notable concentration of surfactant occurring at the interface. We observe both mass conservation and discrete energy dissipation in the experimental results, and they align with our theoretical framework.

4.2. Stability tests

Due to the high-order nonlinear term in the system, severe time step limitations exist on numerical stability. We conduct numerical experiments with different time steps: $\Delta t=1, 0.1$, and 0.01, respectively, to illustrate the stability of our proposed scheme. Then we set the initial conditions as follows:

$$\begin{cases}\phi(x,y,z,0)=0.5+0.01(\text{rand}(x,y,z)-0.5),\\ \psi(x,y,z,0)=0.1+0.05\text{rand}(x,y,z),\quad p(x,y,z,0)=0,\\ u(x,y,z,0)=0.02,\quad v(x,y,z,0)=0,\quad w(x,y,z,0)=0.\end{cases}$$

We use the following set of parameter values for the numerical simulations: $h=0.1$, $\varepsilon=\gamma=0.02$, $M_\phi=M_\psi=0.02$, $\sigma=\varepsilon$, $\xi=0.0001$, $\theta=0.03$, $\nu=1$ regardless of the time step size. As shown in Fig. 3, the numerical solution remains stable without any explosions, and the initial energy values at various time steps do not exhibit an increase over time. This indicates the feasibility of employing larger time steps in numerical simulations. Nonetheless, results obtained by using $\Delta t=0.1$ exhibit similarities to those with a smaller time step, $\Delta t=0.01$, but diverge from those obtained using a larger time step, $\Delta t=1$, requiring significantly more time for convergence. Thus, it is advisable to choose an appropriate value $\Delta t=0.1$ in this and subsequent experiments to balance accuracy and computational efficiency.

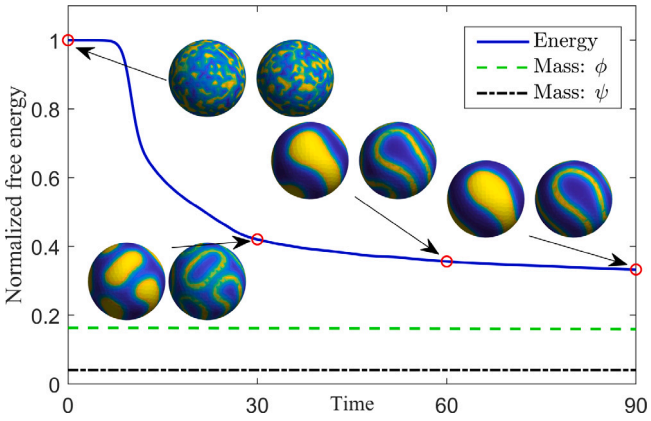

Fig. 2. Evolution of energy dissipation and mass conservation over time of the proposed scheme for a time step size of $\Delta t = 0.1$. The inset figures display the morphology of the phase variable ϕ at specific times(from left to right, representing the results at $t = 0, 30, 60$ and 90, respectively).

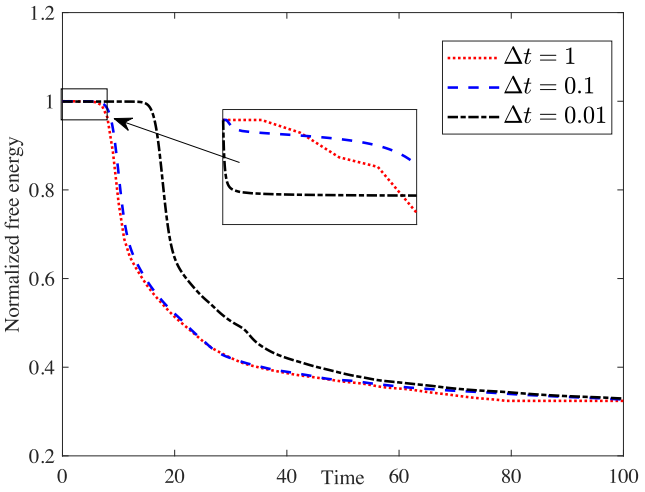

Fig. 3. Temporal evolution of the non-increasing energy functional for the three times step sizes, $\Delta t = 0.01, 0.1$ and 1.

4.3. Convergence test

In this subsection, we conduct convergence tests in time and space to confirm the second-order accuracy of our proposed scheme. To eliminate potential differential effects stemming from manifold topology, we employ unit spheres to produce a collection of high-quality meshes adhering to Delaunay triangle properties. To assess the temporal second-order accuracy, we utilize a distinct set of time steps, specifically Δt = 8e−2, 4e−2, 2e−2, and 1e−2, while maintaining a consistent spatial step of h = 5e−2. These tests run until $t = 10$, utilizing identical initial conditions:

$$\begin{cases} \phi(x,y,z,0) = 0.5 + 0.5\sin(6\pi x)\sin(6\pi y)\sin(6\pi z), \\ \psi(x,y,z,0) = 0.15 + 0.01\text{rand}(x,y,z), \quad p(x,y,z,0) = 0, \\ u(x,y,z,0) = 0, \quad v(x,y,z,0) = 0, \quad w(x,y,z,0) = 0.01. \end{cases}$$

The parameters have been set to $\varepsilon = \gamma = 0.02$, $M_\phi = M_\psi = 0.02$, $\sigma = \varepsilon$, $\xi = 0.0001$, $\theta = 0.03$, $\nu = 1$. Note that such a system has no analytical solution so far, we use the fine-grained time step result Δt = 4e−4 as the reference solution and denote it as ϕ^{ref}. Here, the error is denoted as $e_{i,\Delta t} := \phi_{i,\Delta t} - \phi_i^{\text{ref}}$, while the convergence rate is represented by the ratio of the successive errors, denoted as $\log_2(\|e_{i,\Delta t}\|_2/\|e_{i,\Delta t/2}\|_2)$. As shown in Table 1, the errors and convergence rates can be found demonstrating the quadratic accuracy of the proposed schemes. To present the second-order spatial accuracy of the proposed scheme, we define the error as $e_{i,h} := \phi_{i,d} - (\alpha_i\phi_p^{\text{ref}} + \beta_i\phi_q^{\text{ref}} + \lambda_i\phi_r^{\text{ref}})$, where the weighting coefficients α_i, β_i and λ_i are determined by $\mathbf{v}_{i,d} := \alpha_i\mathbf{v}_p^{\text{ref}} + \beta_i\mathbf{v}_q^{\text{ref}} + \lambda_i\mathbf{v}_r^{\text{ref}}$, and p, q, and r denote the indices of the microreference grid within the triangle. These results are presented in Table 2, where $\log_2(\|e_{i,h}\|_2/\|e_{i,h/2}\|_2)$ represents the convergence rate, with a common time step of $\Delta t = 4e-4$. The reference solution is calculated using a highly refined spatial grid with $h = 0.005$. The information presented in Table 2 shows that the second-order spatial accuracy is achieved.

Table 1
Numerical errors and convergence rates of the phase field variables ϕ and ψ, and the velocity fields u, v, and w using various time steps.

Δt	Error					Order				
	ϕ	ψ	u	v	w	ϕ	ψ	u	v	w
8.0e−02	2.49e−04	1.74e−05	8.55e−05	4.45e−05	1.35e−04	–	–	–	–	–
4.0e−02	6.32e−05	4.41e−06	2.30e−05	1.03e−05	3.52e−05	1.98	1.98	1.90	2.11	1.94
2.0e−02	1.79e−05	1.11e−06	5.48e−06	2.67e−06	8.81e−06	1.82	1.99	2.07	1.94	1.99

Table 2
Numerical errors and convergence rates of the phase field variables ϕ and ψ, and the velocity fields u, v, and w using various space steps.

h	Error					Order				
	ϕ	ψ	u	v	w	ϕ	ψ	u	v	w
0.2	2.87e−03	2.06e−04	4.23e−06	4.26e−06	4.21e−06	–	–	–	–	–
0.1	8.25e−04	5.51e−05	1.11e−06	1.10e−06	1.12e−06	1.80	1.90	1.93	1.95	1.91
0.05	1.33e−04	1.08e−05	2.69e−07	2.69e−07	2.69e−07	2.63	2.34	2.04	2.04	2.05

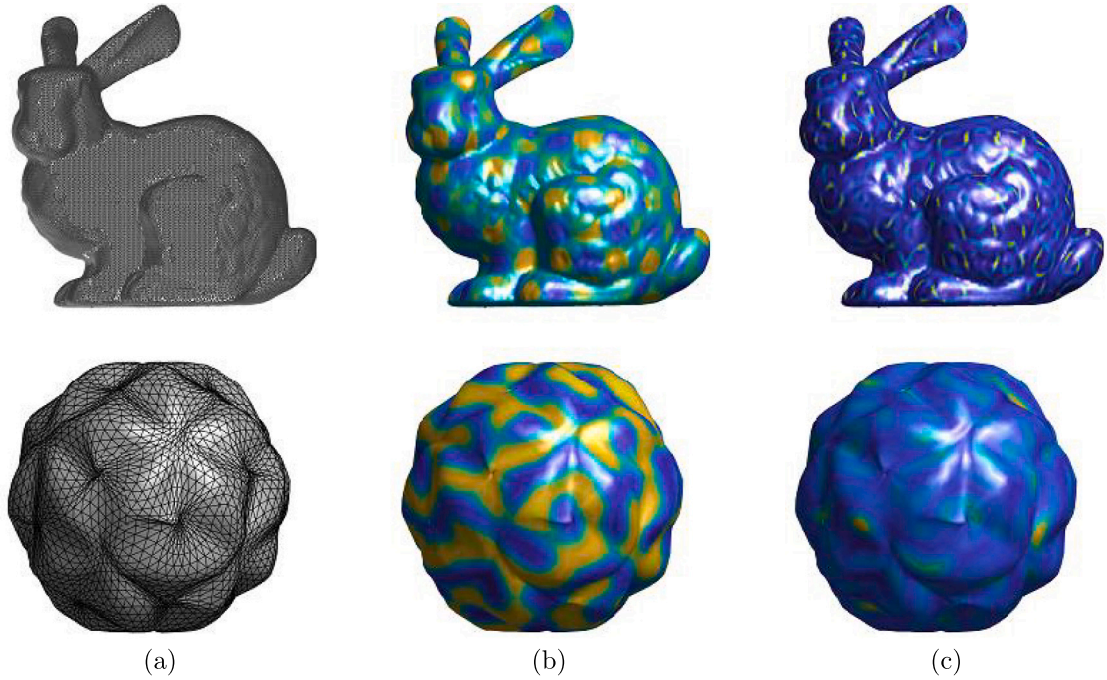

Fig. 4. Separation of phases on different surfaces: computations on a bunny model (top) and a bumpy sphere (bottom). (a) illustrates the triangulation of the irregular meshes. (b) and (c) show the distribution of the fluid phase field ϕ and the surfactant ψ at $t = 0.03$, respectively.

4.4. Phase separation on irregular surface mesh

In this section, we validate the effectiveness and reliability of our discretization algorithm on two irregular curved surface meshes: the surface of a bunny model and a bumpy sphere. The quality of mesh structures often significantly affects the accuracy and precision of computations in conventional surface discretization simulation algorithms. This is particularly evident in discrete divergence, gradient, and Laplace–Beltrami operator calculations, which may challenge the conservativity of the system. Such challenges are commonly encountered in surface discretization simulations. As shown in Fig. 4, we solve the fluid–surfactant system on the aforementioned irregular surfaces to assess the feasibility and accuracy of our algorithm in handling irregular surfaces. The initial conditions are:

$$\begin{cases} \phi(x,y,z,0) = 0.5 + 0.2\sin(10\pi x)\sin(10\pi y)\sin(10\pi z), \\ \psi(x,y,z,0) = 0.35 + 0.05\sin(10\pi x)\sin(10\pi y)\sin(10\pi z) \\ u(x,y,z,0) = 0, \quad v(x,y,z,0) = 0, \quad w(x,y,z,0) = 0.01, \quad p(x,y,z,0) = 0. \end{cases}$$

The parameters chosen for the bunny model surface are $\varepsilon = \gamma = 0.003$, $M_\phi = M_\psi = 0.2$, $\sigma = \varepsilon$, $\xi = 0.0001$, $\theta = 0.1$, $\nu = 2$. For the other bumpy sphere, the parameters selected are $\varepsilon = \gamma = 0.1$, $M_\phi = M_\psi = 0.5$, $\sigma = \varepsilon$, $\xi = 0.0001$, $\theta = 0.1$, $\nu = 2$ The figure displays irregular

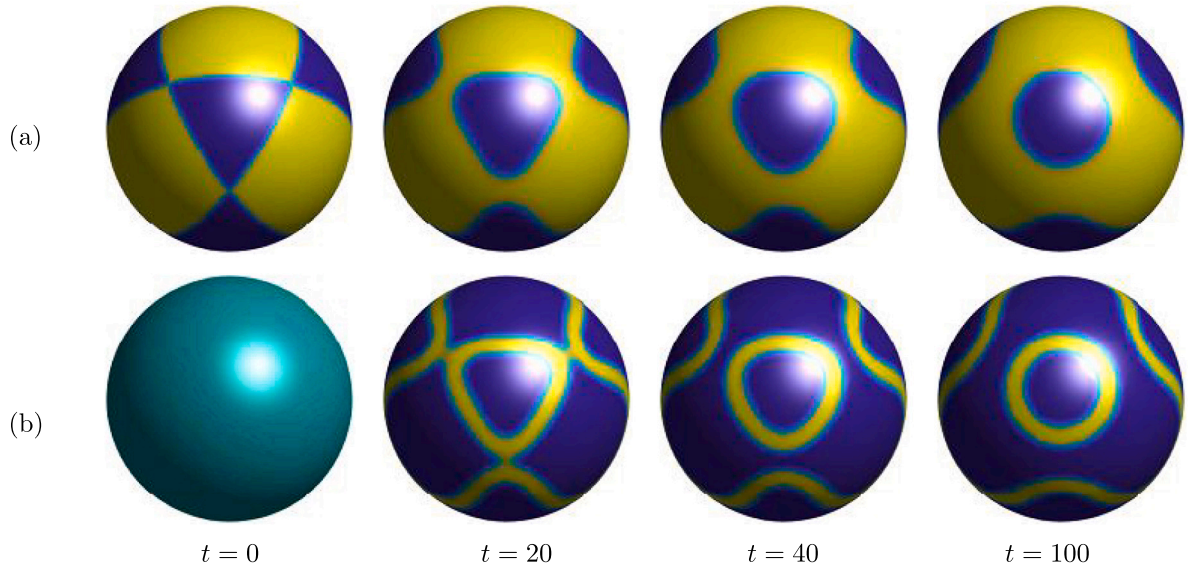

Fig. 5. Temporal evolution of polymerization of three liquid groups in the presence of surfactant at $t = 0, 20, 40$, and 100. The upper and lower subfigures represent phase field variable ϕ and surfactant ψ respectively.

meshes triangulation in Fig. 4(a). Fig. 4(b) and (c) show the distribution of the fluid phase field ϕ and the surfactant ψ at $t = 0.03$, respectively. The results above demonstrate that the phase separation trend of the fluid phase field variable ϕ and the aggregation effect of the surfactant ψ are well captured on the two irregular triangular surface meshes. This suggests that our method can yield physically realistic results even with irregular and low-quality surface meshes.

4.5. Liquid agglomeration test on curved surfaces

In this subsection, we utilize the proposed fluid–surfactant scheme to model the relaxation process of binary phase flow and surfactant on a curved surface. As illustrated in Fig. 5, we simulate the fusion process of three square liquid groups, initially sharing a common vertex on a unit sphere each other. Motivated by surface tension, the adjacent square liquid entities gradually merge over time, causing a concentration of surfactant at the boundary between the two-phase fluids. Consequently, the initially sharp shapes relax into smoother interfaces as this transformation progresses. The initial conditions are:

$$\begin{cases} \phi(x,y,z,0) = 1.5 - 0.5\tanh\left(\dfrac{|x-1|+|y|+|z|-1}{\sqrt{5}\varepsilon}\right) \\ \qquad\qquad - 0.5\tanh\left(\dfrac{|x|+|y-1|+|z|-1}{\sqrt{5}\varepsilon}\right) - 0.5\tanh\left(\dfrac{|x|+|y|+|z-1|-1}{\sqrt{5}\varepsilon}\right), \\ \psi(x,y,z,0) = 0.22, \quad p(x,y,z,0) = 0, \\ u(x,y,z,0) = 0, \quad v(x,y,z,0) = 0, \quad w(x,y,z,0) = 0. \end{cases}$$

The parameters have been set to $\varepsilon = \gamma = 0.02$, $M_\phi = M_\psi = 0.1$, $\sigma = \varepsilon$, $\xi = 0.0001$, $\theta = 0.1$, $\nu = 1$. We conduct this simulation using a time step of $\Delta t = 0.1h$ with a mesh size of $h = 0.1$. The subfigures in Fig. 5 capture snapshots of the phase field variable and surfactant at $t = 0, 20, 40$, and 100, respectively.

4.6. Deformation test under shear flow

In this subsection, we conducted simulations to investigate the deformations of a droplet influenced by shear flow, both in the presence and absence of surfactant. The initial conditions were set as:

$$\begin{cases} \phi(x,y,z,0) = 0.5 + 0.5\tanh\left(\dfrac{\sqrt{(x-1)^2+y^2+z^2}-0.5}{\sqrt{2}\varepsilon}\right), \\ \psi(x,y,z,0) = 0.22, \quad p(x,y,z,0) = 0, \\ u(x,y,z,0) = 0, \quad v(x,y,z,0) = 0, \quad w(x,y,z,0) = 0, \end{cases}$$

Subsequently, with parameters $\varepsilon = \gamma = 0.02$, $M_\phi = 0.5$, $M_\psi = 0.1$, $\sigma = \varepsilon$, $\xi = 0.0001$, $\theta = 0.1$, $\nu = 1$. We conduct this simulation using a time step of $\Delta t = 0.1$ and a mesh size of $h = 0.1$. Fig. 6 displays the shape of the droplet under the effect of shear flow as

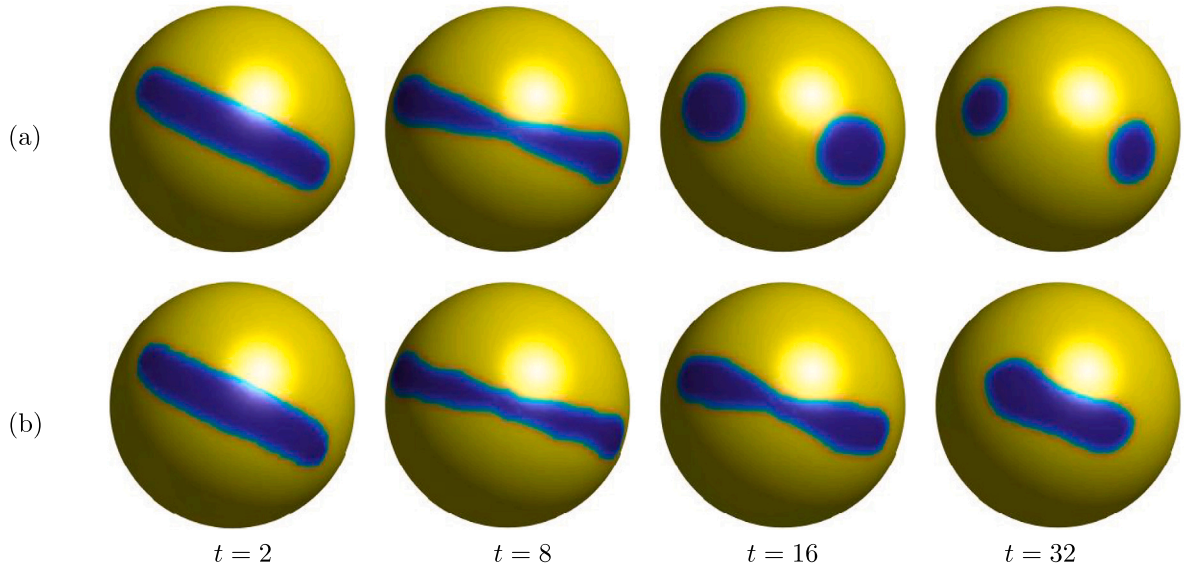

Fig. 6. (a) Depicts the temporal evolution of the phase field variable under shear flow without the influence of any surfactant. (b) Illustrates controlled tests of (a) with the influence of a surfactant. The specified time instances are $t = 2$, 8, 16, and 32.

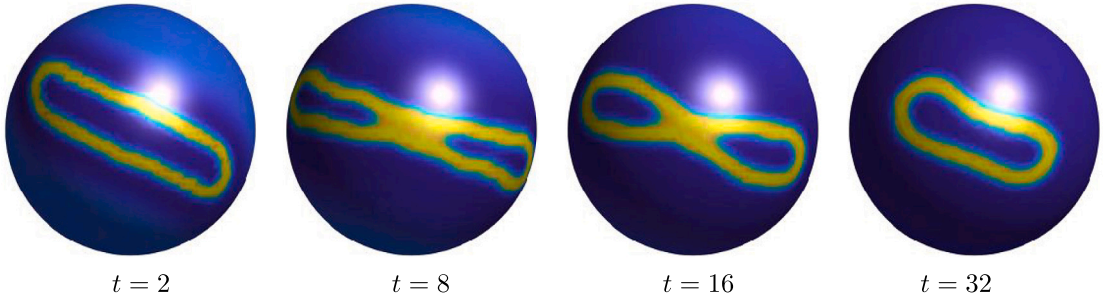

Fig. 7. The evolution of the surfactant over time under the effect of shearflow, corresponding to the phase field variable ϕ in Fig. 6(b), with snapshots at $t = 2, 8, 16$ and 32, respectively.

obtained through the proposed scheme. As shown in Fig. 6(a), snapshots of the droplet affected by shear flow are shown at time instances $t = 2, 8, 16$, and 32, without surfactant. Fig. 6(b) presents the scenario with surfactant at the same time points. The top subfigure shows that at $t = 16$, the droplet tip breaks due to high velocity and minimal surface tension. Contrarily, in the presence of surfactant surface tension, the droplet remains intact without any breakage, as illustrated in Fig. 6(b). In Fig. 7, snapshots of the surfactant distribution at corresponding moments are provided. Moreover, in Fig. 8, snapshots of velocity field and pressure field on a surface at different moments are provided. These observations showcase the consistency of the proposed scheme with the anticipated physical behavior.

4.7. Spinodal decomposition

In this subsection, we examine the evolution of phase separation under various initial conditions on curved surface, considering a homogeneous binary mixture. The system evolves from a uniform state to a two-phase state as concentration fluctuations spontaneously grow. Parameters are chosen as $\varepsilon = \gamma = 0.02$, $M_\phi = 0.5$, $M_\psi = 0.1$, $\sigma = \varepsilon$, $\xi = 0.0001$, $\theta = 0.1$, $\nu = 2$, with initial conditions

$$\begin{cases} \phi(x, y, z, 0) = \bar{\phi}_0 + 0.01\text{rand}(x, y, z) \\ \psi(x, y, z, 0) = 0.15 + 0.01\text{rand}(x, y, z), \quad p(x, y, z, 0) = 0, \\ u(x, y, z, 0) = 0, \quad v(x, y, z, 0) = 0, \quad w(x, y, z, 0) = 0. \end{cases}$$

We conduct these simulations using the same time step of $\Delta t = 0.1h$ with $h = 0.1$. To visualize the evolution of phase field variables and surfactant under different phase field concentration ratios $\bar{\phi}_0$, snapshots at time $t = 0$, 1, 2, 4, and 8 are presented in Figs. 9, 10, and 11, respectively. In the case of a homogeneous two-phase fluid mixture, phase separation is evident as concentration fluctuations

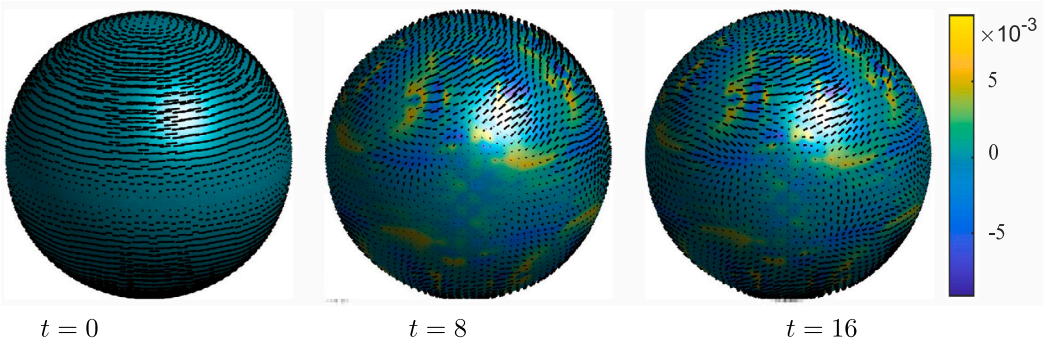

Fig. 8. Snapshots of velocity field and pressure field on a surface at $t = 0$, $t = 8$, and $t = 16$, respectively.

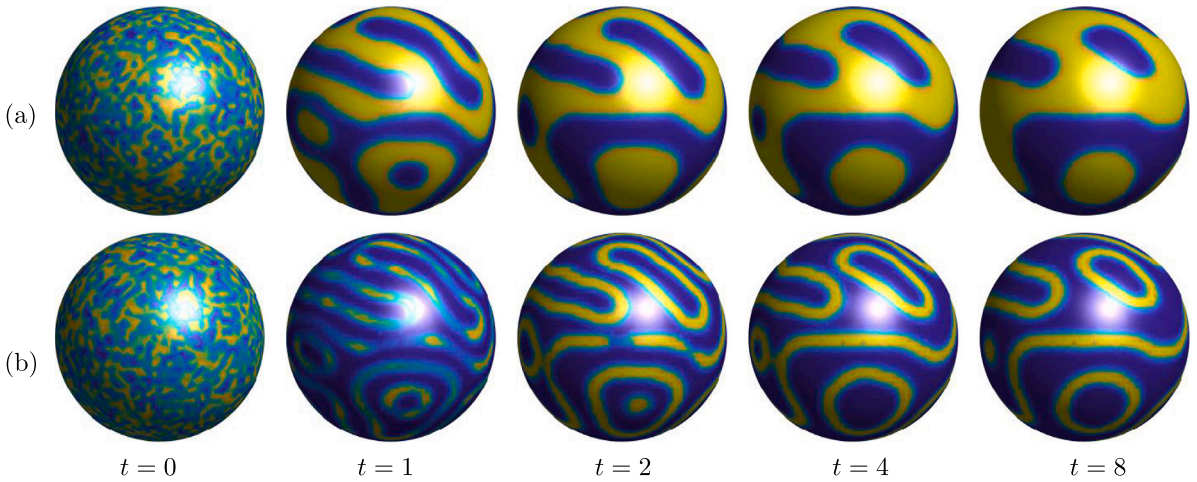

Fig. 9. Temporal evolution for $\bar{\phi} = 0.5$. The upper and lower subfigures depict snapshots of the phase field variable ϕ and surfactant ψ at $t = 0, 1, 2, 4$, and 8, respectively.

increase. Due to surface tension effects, the binary mixture starts to decompose and forms a two-phase interface soon after phase separation initiates. The system transitions from homogeneity to a clear two-phase state. In the case where $\bar{\phi}_0 = 0.5$ (Fig. 9), the two fluids are uniformly mixed with equal masses, resulting in the emergence of a continuous network pattern. As surface tension influences the system, the interface merges to form a distinct two-phase state. When $\bar{\phi}_0 = 0.6$ (Fig. 10), an uneven composition results in a pattern where the fluid with a higher component concentration (yellow) encircles the fluid with a lower component concentration (blue), promoting the formation of fine droplets. As the system minimizes its total energy, these isolated droplets either merge or increase in size. Similarly, for $\bar{\phi}_0 = 0.25$ (Fig. 11), the portion of blue fluid with a high concentration also dominates most of the surface and surrounds the other part. As the system minimizes its total energy, the corresponding isolated droplets thicken or merge. Collectively, the results derived from these simulations share similar traits to the findings discussed in [24,28,32,34], thereby reinforcing the suitability and applicability of our scheme on curved surfaces.

5. Conclusion

In this paper, we introduced an effective approach for simulating fluid–surfactant evolution on curved surfaces. We combined the water–oil–surfactant system, based on the phase field model, with the incompressible NS equation. We adapted the consistency-enhanced SAV method and the projection method into a linear system suitable for biconjugate gradient stabilization techniques. We formulated discrete differential operators applicable to a wide range of surfaces. These operators consistently demonstrated verified second-order accuracy in spatial discretization. To achieve second-order temporal accuracy, we employed a discretization method similar to the Crank–Nicolson approach for the solution equation. The unconditional stability of the discretized system means it is free from time step restrictions. We validated the energy stability of this system and confirmed the second-order accuracy of our discretization approach through various numerical experiments. Compared to alternative algorithms, the approach introduced in this article achieved superior accuracy while significantly reducing computational demands. By utilizing surface data exclusively, it avoided the need for extensive calculations throughout the entire three-dimensional space. The algorithm presented in this article has several limitations, which have be outlined as the following:

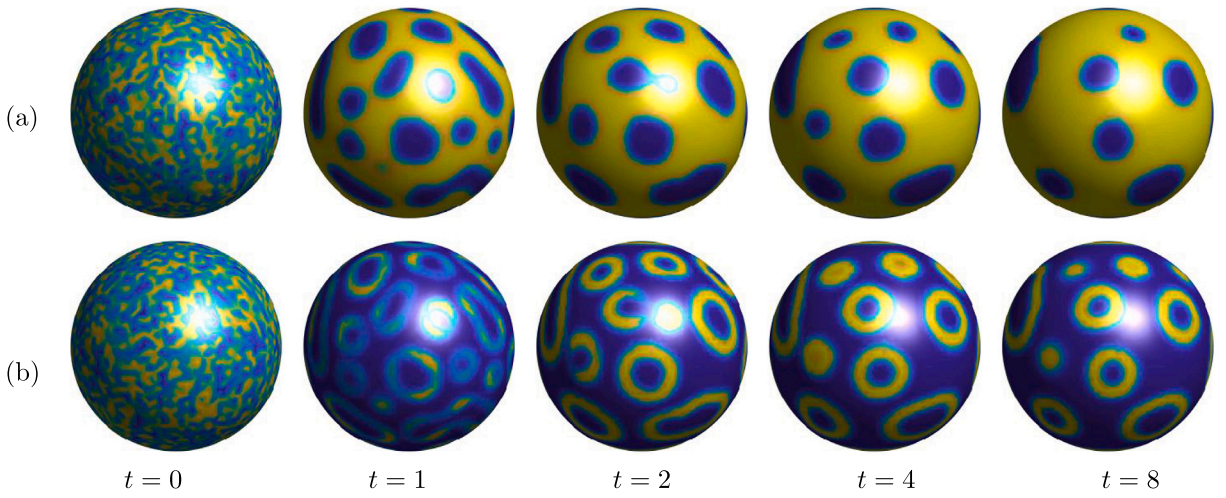

Fig. 10. Temporal evolution for $\bar{\phi} = 0.6$. The upper and lower subfigures depict images capturing the phase field variable ϕ and surfactant ψ at $t = 0, 1, 2, 4,$ and 8, respectively.

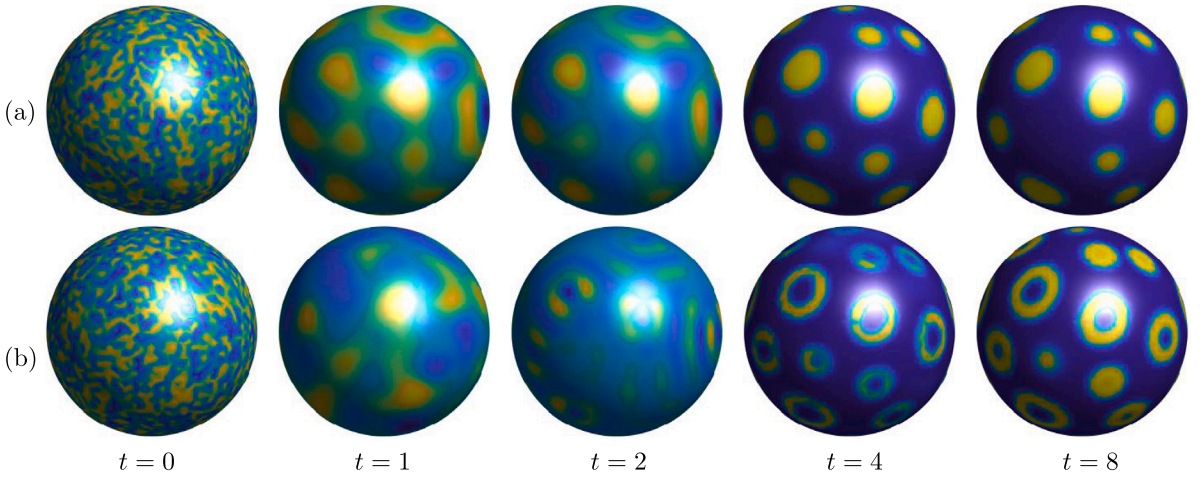

Fig. 11. Temporal evolution for $\bar{\phi} = 0.25$. The upper and lower subfigures depict images capturing the phase field variable ϕ and surfactant ψ at $t = 0, 1, 2, 4,$ and 8, respectively.

- The effectiveness of this algorithm relies heavily on the quality of the surface mesh. Insufficient mesh quality, especially if it does not conform to Delaunay decomposition, can greatly undermine the accuracy of numerical computations.
- The computational complexity of this algorithm is noteworthy, necessitating meticulous attention to grid point coordinates and their interconnections, which directly correlates with the volume of grid data.
- Meeting elevated spatial accuracy criteria necessitates the redefinition of discrete space operators, a task that inherently poses greater difficulty.

CRediT authorship contribution statement

Bing Jiang: Writing – original draft, Visualization, Software, Methodology, Investigation, Conceptualization. **Qing Xia:** Writing – review & editing, Methodology, Conceptualization. **Junseok Kim:** Supervision, Methodology. **Yibao Li:** Writing – review & editing, Supervision, Software, Project administration, Methodology, Conceptualization.

Declaration of competing interest

The authors declare that there is no conflict of interests regarding the publication of this article.

Data availability

No data was used for the research described in the article.

Acknowledgments

Y.B. Li is supported by National Natural Science Foundation of China (No. 12271430). The authors would like to thank the reviewers for their constructive and helpful comments regarding the revision of this article.

References

[1] Iglauer S, Wu Y, Shuler P, Tang Y, Goddard WA. New surfactant classes for enhanced oil recovery and their tertiary oil recovery potential. J Pet Sci Eng 2010;71:23–9.
[2] Fonseca I, Morini M, Slastikov V. Surfactants in foam stability: A phase-field model. Arch Ration Mech Anal 2007;183:411–56.
[3] Li Y, Guo S. Triply periodic minimal surface using a modified allen-cahn equation. Appl Math Comput 2017;295:84–94.
[4] Li Y, Liu R, Xia Q, He C, Li Z. First-and second-order unconditionally stable direct discretization methods for multi-component Cahn–Hilliard system on surfaces. J Comput Appl Math 2022;401:113778.
[5] Myers D. Surfactant science and technology. third ed.. Hoboken: Wiley; 2006.
[6] Xia Q, Jiang X, Li Y. A modified and efficient phase field model for the biological transport network. J Comput Phys 2023;488:112192.
[7] Li Y, Kim J. A comparison study of phase-field models for an immiscible binary mixture with surfactant. Eur Phys J B 2012;85:340.
[8] Yang X, Ju L. Linear and unconditionally energy stable schemes for the binary fluid-surfactant phase fieldmodel. Comput Methods Appl Mech Engrg 2017;318:1005–29.
[9] Li Y, Yun A, Lee D, Shin J, Jeong D, Kim J. Three-dimensional volume-conserving immersed boundary model for two-phase fluid flows. Comput Methods Appl M 2013;257:36–46.
[10] Gu S, Zhang H, Zhang Z. An energy-stable finite-difference scheme for the binary fluid-surfactant system. J Comput Phys 2014;270:416–31.
[11] Li Y, Zhang L, Xia Q, Yu Q, Kim J. An unconditionally energy-stable second-order time-accurate numerical scheme for the coupled Cahn–Hilliard system in copolymer/homopolymer mixtures. Comput Mater Sci 2021;200:110809.
[12] Yang X. Numerical approximations for the Cahn-Hilliard phase field model of the binary fluid-surfactant system. SIAM J Sci Comput 2018;74:1533–53.
[13] Cheng J, Xia Q, Kim J, Li Y. An efficient linear and unconditionally stable numerical scheme for the phase field sintering model. Commun Nonlinear Sci Numer Simul 2023;127:107529.
[14] Cahn JW, Hilliard JE. Free energy of a nonuniform system. I Interfacial Free Energy, J Chem Phys 1958;28:258–67.
[15] Xia Q, Sun G, Yu Q, Kim J, Li Y. Thermal-fluid topology optimization with unconditional energy stability and second-order accuracy via phase-field model. Commun Nonlinear Sci Numer Simul 2023;116:106782.
[16] Xia B, Mei C, Yu Q, Li Y. A second order unconditionally stable scheme for the modified phase field crystal model with elastic interaction and stochastic noise effect. Comput Methods Appl Mech Engrg 2020;363:112795.
[17] Yu Q, Xia Q, Li Y. A phase field-based systematic multiscale topology optimization method for porous structures design. J Comput Phys 2022;466:111383.
[18] Xia Q, Sun G, Kim J, Li Y. Multi-scale modeling and simulation of additive manufacturing based on fused deposition technique. Phys Fluids 2023;35:3.
[19] Laradji M, Guo H, Grant M, Zuckermann MJ. The effect of surfactants on the dynamics of phase separation. J Phys Condens: Matter 1992;4(32):6715.
[20] van der Sman R, van der Graaf S. Diffuse interface model of surfactant adsorption onto flat and droplet interfaces. Rheol Acta 2006;46(1):3–11.
[21] Teng CH, Chern IL, Lai MC, et al. Simulating binary fluid-surfactant dynamics by a phase field model. Discrete Contin Dyn Syst B 2012;17:1289–307.
[22] Zhu G, Kou J, Sun S, Yao J, Li A. Decoupled, energy stable schemes for a phase-field surfactant model. Comput Phys Comm 2018;233:67–77.
[23] Xu C, Chen C, Yang X. Efficient, non-iterative, and decoupled numerical scheme for a new modified binary phase-field surfactant system. Numer Algorithms 2021;86:863–85.
[24] Yang J, Kim J. An improved scalar auxiliary variable (SAV) approach for the phase-field surfactant model. Appl Math Model 2021;90:11–29.
[25] Yang J, Kim J. A variant of stabilized-scalar auxiliary variable (S-SAV) approach for a modified phase-field surfactant model. Comput Phys Comm 2021;261:107825.
[26] Kim J, Kang K, Lowengrub J. Conservative multigrid methods for Cahn-Hilliard fluids. J Comput Phys 2004;193:511–43.
[27] Shen J. On error estimates of projection methods for Navier–Stokes equations: first-order schemes. SIAM J Numer Anal 1992;29:57–77.
[28] Zhu G, Kou J, Sun S, Yao J, Li A. Numerical approximation of a phase-field surfactant model with fluid flow. SIAM J Sci Comput 2019;80:223–47.
[29] Gross S, Jankuhn T, Olshanskii MA, Reusken A. A trace finite element method for vector-laplacians on surfaces. SIAM J Numer Anal 2018;56:2406–29.
[30] Olshanskii MA, Quaini A, Reusken A, Yushutin V. A finite element method for the surface Stokes problem. SIAM J Sci Comput 2018;40:A2492–518.
[31] Wang C, Guo Y, Zhang Z. Unconditionally energy stable and bound-preserving schemes for phase-field surfactant model with moving contact lines. J Sci Comput 2022;92:20.
[32] Sun M, Feng X, Wang K. Numerical simulation of binary fluid-surfactant phase field model coupled with geometric curvature on the curved surface. Comput Methods Appl Mech Engrg 2020;367:113123.
[33] Pan Q, Chen C, Rabczuk T, Zhang J, Yang X. The subdivision-based IGA-EIEQ numerical scheme for the binary surfactant Cahn-Hilliard phase-field model on complex curved surfaces. Comput Methods Appl Mech Engrg 2023;406:115905.
[34] Sun M, Xiao X, Feng X, Wang K. Modeling and numerical simulation of surfactant systems with incompressible fluid flows on surfaces. Comput Methods Appl Mech Engrg 2022;390:114450.
[35] Huang S, Xiao X, Feng X. An adaptive time-stepping method for the binary fluid-surfactant phase field model on evolving surfaces. J Sci Comput 2023;95(1):29.
[36] Xia Q, Yu Q, Li Y. A second-order accurate, unconditionally energy stable numerical scheme for binary fluid flows on arbitrarily curved surfaces. Comput Methods Appl Mech Engrg 2021;384:113987.
[37] Xia Q, Liu Y, Kim J, Li Y. Binary thermal fluids computation over arbitrary surfaces with second-order accuracy and unconditional energy stability based on phase-field model. J Comput Appl Math 2023;433:115319.
[38] Li Y, Yang J. Consistency-enhanced SAV BDF2 time-marching method with relaxation for the incompressible Cahn–Hilliard–Navier–Stokes binary fluid model. Commun Nonlinear Sci Numer Simul 2023;118:107055.
[39] Han D, Brylev A, Yang X, Tan Z. Numerical analysis of second-order, fully discrete energy stable schemes for phase field models of two-phase incompressible flows. SIAM J Sci Comput 2017;70:965–89.
[40] Li Y, Luo C, Xia B, Kim J. An efficient linear second-order unconditionally stable direct discretization method for the phase-field crystal equation on surfaces. Appl Math Model 2019;67:477–90.
[41] Gong Y, Zhao J, Wang Q. An energy stable algorithm for a quasi-incompressible hydrodynamic phase-field model of viscous fluid mixtures with variable densities and viscosities. Comput Phys Comm 2017;219:20–34.

[42] Yang X. Numerical approximations of the Navier–Stokes equation coupled with volume-conserved multi-phase-field vesicles system: fullydecoupled, linear, unconditionally energy stable and second-order time-accurate numerical scheme. Comput Methods Appl Mech Engrg 2021;375:113600.
[43] Yang X. A novel fully-decoupled, second-order and energy stable numerical scheme of the conserved Allen-Cahn type flow-coupled binary surfactant model. Comput Methods Appl Mech Engrg 2021;373:113502.
[44] Yang X. Fully-discrete spectral-Galerkin scheme with decoupled structure and second-order time accuracy for the anisotropic phase-field dendritic crystal growth model. Int J Heat Mass Transfer 2021;180:121750.
[45] Ye Q, Ouyang Z, Chen C, Yang X. Efficient decoupled second-order numerical scheme for the flow-coupled Cahn-Hilliard phase-field model of two-phase flows. J Comput Appl Math 2022;405:113875.
[46] Jiang M, Zhang Z, Zhao J. Improving the accuracy and consistency of the scalar auxiliary variable (SAV) method with relaxation. J Comput Phys 2022;456:110954.
[47] Yang J, Tan. J. Kim Z. Linear and fully decoupled scheme for a hydrodynamics coupled phase-field surfactant system based on a multiple auxiliary variable approach. J Comput Phys 2022;452:110909.
[48] Chen SG, Wu JY. Discrete conservation laws on curved surfaces. SIAM J Sci Comput 2013;36:719–39.
[49] Chen SG, Wu JY. Discrete conservation laws on curved surfaces II: a dual approach. SIAM J Sci Comput 2014;36:1813–30.
[50] Chen SG, Wu JY. Discrete conservation laws on evolving surfaces. SIAM J Sci Comput 2016;38:1725–42.
[51] Dong L, Wang C, Wise SM, Zhang Z. A positivity-preserving, energy stable scheme for a ternary Cahn-Hilliard system with the singular interfacial parameters. J Comput Phys 2021;442:110451.
[52] Wang M, Huang Q, Wang C. A second order accurate scalar auxiliary variable (SAV) numerical method for the square phase field crystal equation. J Sci Comput 2021;88(2):33.
[53] Cheng Q, Wang C. Error estimate of a second order accurate scalar auxiliary variable (SAV) numerical method for the epitaxial thin film equation. Adv Appl Math Mech 2021;13(6):1318–54.